THE STRESS CORROSION SUSCEPTIBILITY OF STRESS COINED FASTENER HOLES IN AIRCRAFT STRUCTURES

A THESIS

Presented to

The Faculty of the Division of Graduate

Studies and Research

by

Aubrey Edward Carter

In Partial Fulfillment

of the Requirements for the Degree

Master of Science in Aerospace Engineering

Georgia Institute of Technology

November, 1973

THE STRESS CORROSION SUSCEPTIBILITY OF

STRESS COINED FASTENER HOLES IN AIRCRAFT STRUCTURES

Approved: _____

_____

_____

_____

_____

Date approved by Chairman Nov 27, 1973

DEDICATED

To my loving wife and honorable parents for their moral support for the author in completing this thesis.

ACKNOWLEDGEMENTS

The author would like to acknowledge the professional guidance given to him by his thesis advisor, Professor Sathyanarayana V. Hanagud, School of Aerospace Engineering, whose guidance throughout the thesis research was stimulating and helpful. The author is also indebted to Dr. Robert L. Carlson, School of Aerospace Engineering, and to Dr. Jerry M. Anderson, School of Engineering Science and Mechanics, who served on the reading committee and from whom the author received valuable suggestions and advice. Gratitude is also offered to Delta Air Lines, Inc., the author's employer, for giving the author the opportunity to pursue the thesis research. And thanks are given to Mrs. Billie Bellamy, who typed this thesis.

TABLE OF CONTENTS

LIST OF ILLUSTRATIONS

Figure Page

NOTATIONS

σ_y	Yield strength
$\sigma_{o_{ys}}$	Yield strength physical constant
K_y	Yield strength physical constant
l	Measure of grain diameter
W_e	Stored elastic strain energy
W_s	Surface energy
c	Crack half size (Chapter I)
E	Young's Modulus
π	Pi
γ_s	True surface energy
σ_c	Critical stress for unstable crack propagation
σ_r	Radial principal stress
σ_θ	Tangential principal stress
r	Radius or radial distance
α	Radial angle
a	Expanded hole size radius
b	Elastic-plastic boundary
ϵ_r	Radial strain in polar coordinates
ϵ_{r_p}	Radial plastic strain in polar coordinates
$\epsilon_{r_{ep}}$	Elastic part of the total plastic strain in polar coordinates
ϵ_θ	Tangential strain in polar coordinates
ϵ_{θ_p}	Tangential plastic strain in polar coordinates
$\epsilon_{\theta_{ep}}$	Elastic part of the total plastic strain in polar coordinates

ϵ_z	Axial strain
u_r	Radial displacement
u_{rp}	Plastic radial displacement
u_{rep}	Elastic radial displacement
u_o	Final radial displacement
u_{oe}	Limit elastic radial displacement
$\sigma_{\theta p}$	Tangential plastic stress
σ_{rp}	Radial plastic stress
$\sigma_{\theta e}$	Tangential elastic stress
σ_{re}	Radial plastic stress
$\sigma_{\theta TP}$	Total plastic tangential stress
σ_{rTP}	Total plastic radial stress
λ	Plastic flow function
ν	Poisson's ratio
η	Incremental radial displacement
C_1, C_2, C_3, C_4, C_5, C_6, C_7, C_8, C_9, f	Constants

SUMMARY

The cold working process of stress coining is used to provide fatigue improvement of fastener holes in aircraft structures. The cold working produces a radial flow of the metal. The residual stresses resulting from stress coining provide protection against fatigue damage by opposing the applied tensile stresses in service at the edge of the fastener hole. However, it has been shown analytically in this thesis that adjacent to the compressively stressed region surrounding the stress coined hole, there is a zone stressed in sustained tension. This residual tensile stress can have a deleterious effect on the stress corrosion susceptibility of the postcoined structure.

The problem of the susceptibility to stress corrosion cracking of AISI 7075-T651 aluminum alloy, a commonly used aircraft high-strength structural material, has been examined theoretically and experimentally. The elastic-plastic analysis shows that the short transverse stress corrosion threshold level is exceeded by the residual stresses produced by the stress coining process. Alternate immersion corrosion testing, metallographic examination and electron fractography have been used to investigate the stress corrosion susceptibility experimentally.

CHAPTER I

INTRODUCTION

Stress Coining

Aircraft structural members are susceptible to fatigue cracking at fastener holes under cyclic loading conditions (1). Many aircraft parts containing fastener holes are stress coined prior to assembly, or subsequently, to lower this susceptibility to cracking in fatigue-prone areas (2). Stress coining is a cold working process that consists of expanding holes in structural members by pulling an oversized mandrel hydraulically through the fastener holes as illustrated in Figure 1.

The process of drawing the mandrel through the fastener holes results in a radial flow of the metal. The residual stresses resulting from the operation in the region surrounding the holes provide protection against fatigue damage by opposing the applied tensile stresses and acting as an obstacle to crack initiation (3). Adjacent to the compressively stressed region, however, there is a zone under sustained tensile stress*. Although the tensile stress does not affect the fatigue properties of the part, its deleterious effect on the stress corrosion susceptibility of high-strength aluminum alloys under adverse grain orientation can result in cracking of parts in service.

Many load carrying members in structural assemblies of aircraft are machined from high-strength aluminum plate stock. For optimum

*This has been discussed in Chapter III.

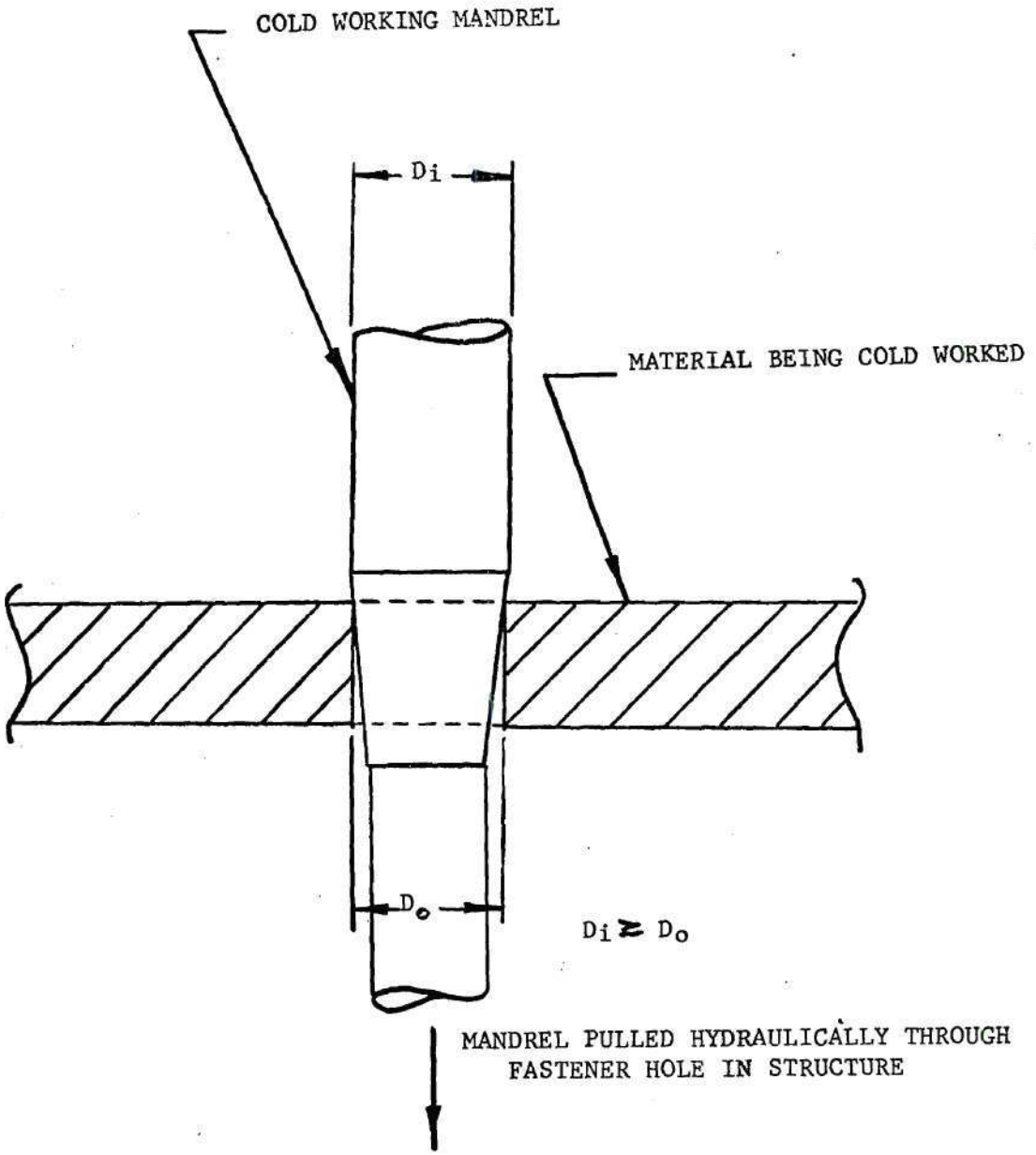

Figure 1. Schematic of Stress Coining process

static tensile properties, the longitudinal direction of the plate is usually aligned with the principal tensile stressed direction of the structure (4). Structures with the rolling direction aligned in this manner benefit from grain size strengthening due to the smaller effective grain size according to the Hall-Petch relation (5):

$$\sigma_y = \sigma_{oys} + K_y\, l^{-\frac{1}{2}} \qquad (1.1)$$

where $\sigma_y \sim$ yield strength

σ_{oys} and $K_y \sim$ physical constants

$l \sim$ measure of grain diameter

Structures stressed perpendicular to the rolling direction are weakened by the alignment of inclusions in the longitudinal direction and by the larger grain size.

Therefore, for common structural cross section shapes (such as I-beams with their axes aligned with the rolling direction), the fastener holes may be located in the longitudinal short transverse plane as illustrated in Figure 2. When these fastener holes are stress coined for fatigue improvement, the sustained tensile load resulting from the stress coining process stresses the short transverse grains. It has been shown that the threshold stress to cause stress corrosion cracking in short transverse smooth specimens of AISI 7075-T651 aluminum, a commonly used aircraft high-strength structural material, is approximately seven ksi (6). Therefore, stress corrosion cracks may initiate under suitable environmental conditions in any exposed area where the short transverse tensile stresses are greater than seven ksi.

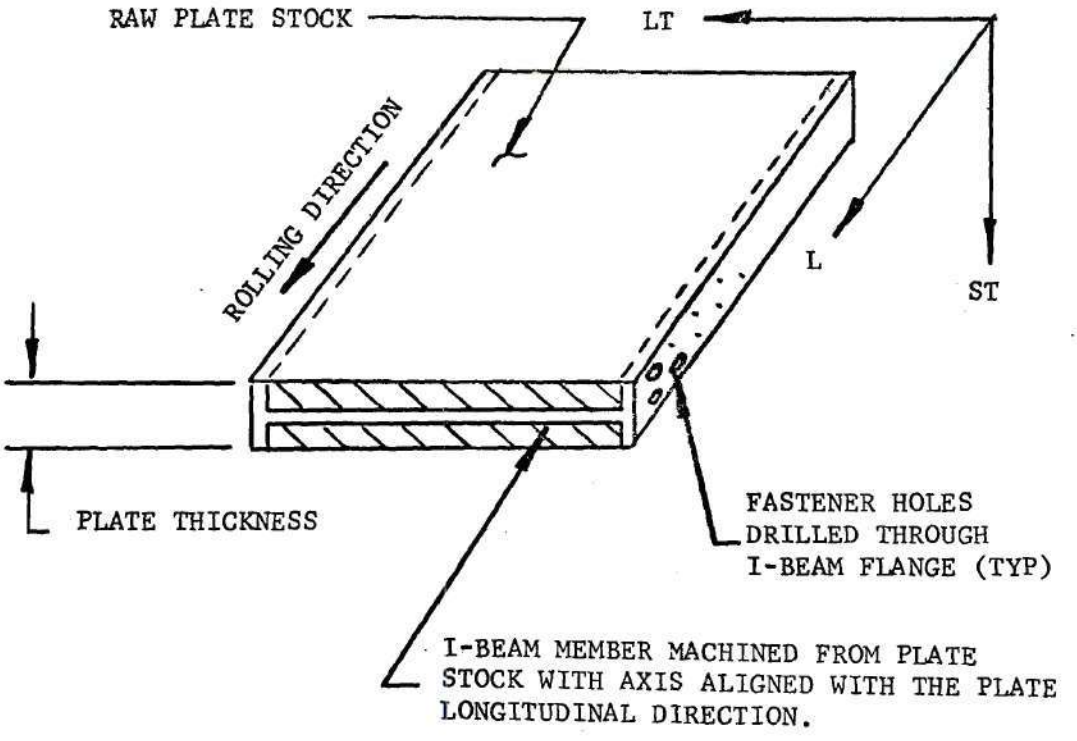

(A) ORIENTATION OF MACHINING TYPICAL AIRCRAFT "I-BEAM" STRUCTURE.

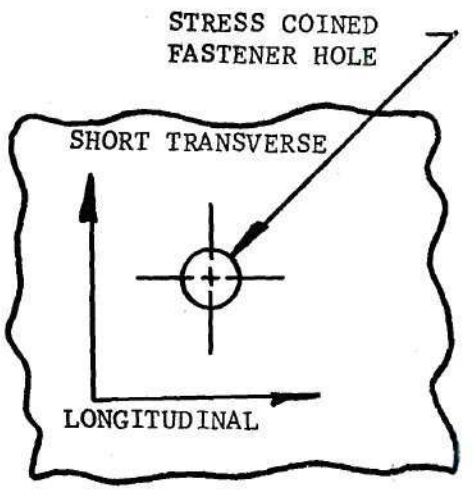

(B) DETAIL OF TYPICAL FASTENER HOLE.

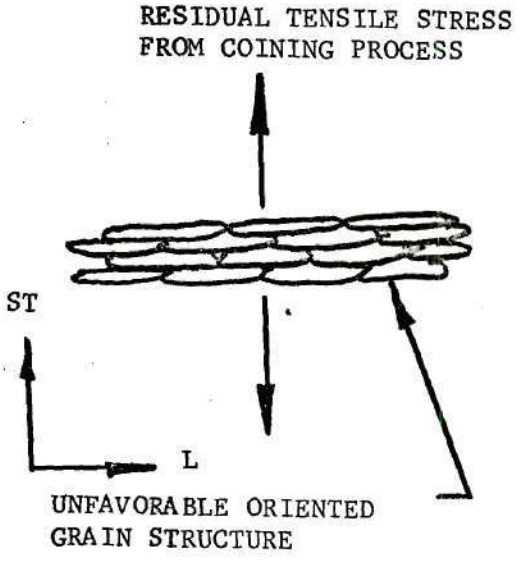

(C) DIRECTION OF GRAIN STRESSING AROUND COINED FASTENER HOLE.

Figure 2. Typical Aircraft Structural Part Machined from Plate Stock.

Stress Corrosion Cracking in Aluminum Alloys

Stress corrosion cracking has been defined as: "Spontaneous failure by cracking of a metal under the combined action of sustained stress and corrosion." (7). This definition was expanded later to the following: "Susceptibility of a metal to stress corrosion implies a greater deterioration in the mechanical properties of a material through the simultaneous action of a static stress and exposure to a corrosive environment than would occur by the separate but additive action of those agencies." (8).

The stress corrosion cracking process requires not only a susceptible alloy, but the combination of a certain microstructure, a sustained tensile stress and exposure to particular types of environments. Each of these conditions are inseparably involved in the stress corrosion process.

In aluminum alloys, stress corrosion cracking typically occurs along the grain boundaries in contrast to the transgranular cracking generally associated with fatigue, creep rupture, tensile overload, etc. (9). When viewed using an electron microscope, the stress corrosion fracture surface may be characterized by the intergranular path with multiple secondary cracking around the grains. Corrosion products are frequently observed on stress corrosion fractures and may be identified using X-ray flourescence. Electron fractography photomicrographs shown in Figures 3 through 5 illustrate the fracture surface appearance of stress corrosion, in contrast to that of fatigue and ductile rupture of typical service of an Al-Zn-Mg-Cu alloy (see following pages):

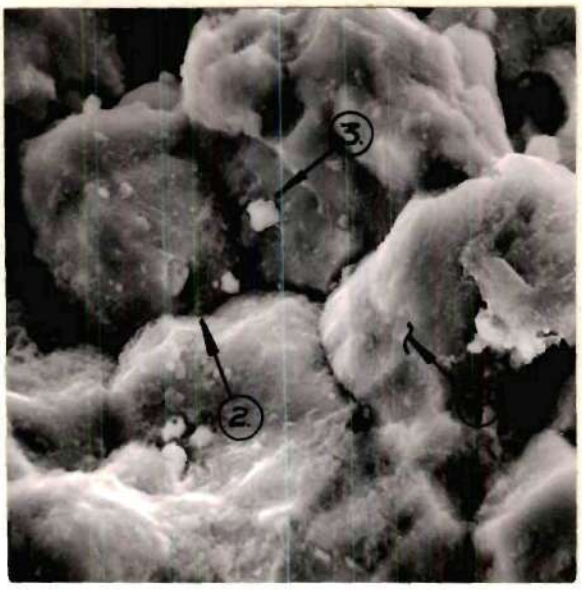

(Magnification 2000X)

DISTINGUISHING FEATURES:

1. Intergranular path of primary crack giving irregular fracture appearance.

2. Multiple secondary intergranular cracking.

3. Corrosion products appearing on fracture surface.

Figure 3. Scanning Electron Fractograph of Stress Corrosion Fracture in Al-Zn-Mg-Cu Alloy

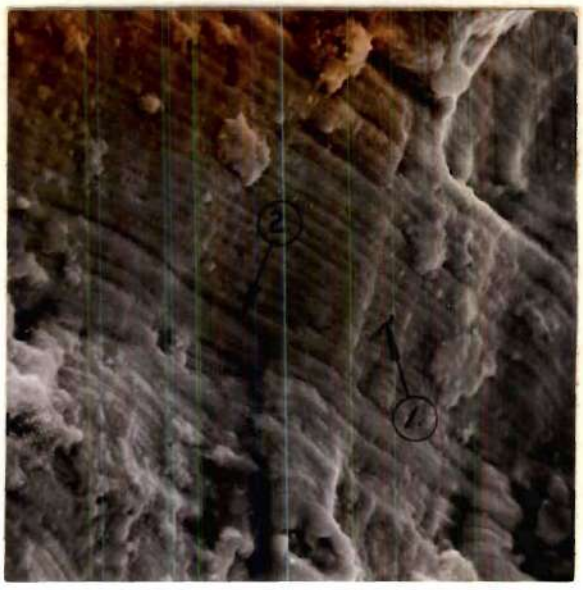

(Magnification 1100X)

DISTINGUISHING FEATURES:

1. Transgranular path of crack giving smooth fracture appearance.

2. Striations on fracture surface caused by cylic crack propagation.

Figure 4. Scanning Electron Fractograph of Fatigue Cracking in Al-Zn-Mg-Cu Alloy

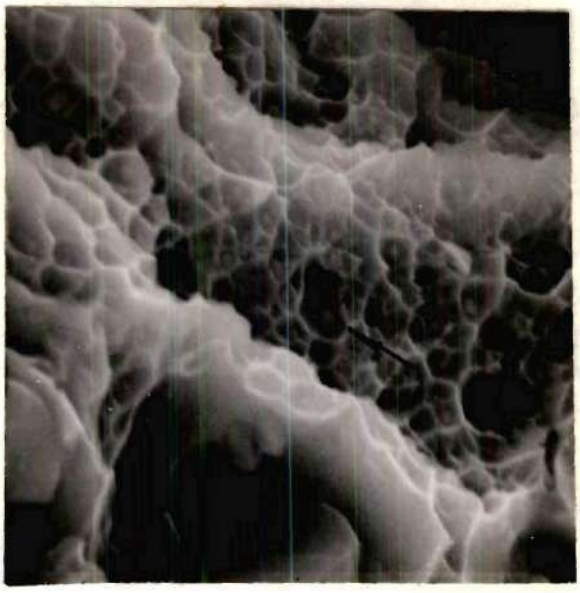

(Magnification 2200X)

DISTINGUISHING FEATURES:

Formation of microvoids or "dimples" on the grain surfaces and microvoid coalescence. Equiaxed dimples indicate tensile overstress.

Figure 5. Scanning Electron Fractograph of Ductile Rupture in Al-Zn-Mg-Cu Alloy

Fatigue cracking in aluminum is typically transgranular with striations caused by the cylic crack propagation. Ductile rupture is characterized by microvoids or "dimples" on the fracture surface. The fracture path may be intragranular or intergranular.

Because stress corrosion in susceptible aluminum alloys is invariably intergranular, the occurrence of intergranular corrosion may be confused with stress corrosion. "Intergranular corrosion" often causes susceptible alloys to delaminate by exfoliation. For the metal degradation to be called "stress corrosion," an accelerating effect of stress must be demonstrated (10).

General Mechanisms

Many theories have been proposed to describe the general mechanisms of stress corrosion cracking. Two of the well accepted theories can be classified as the following: (1) electrochemical or (2) stress sorption cracking. There are numerous other theories put forth on this subject.

The Electrochemical Theory. The electrochemical theory (11) is based on potential measurements in various aluminum alloys showing that intergranular crack paths were anodic to the grains. The theory proposes that galvanic cells are established between continuous intermetallic precipitates and adjacent metal at grain boundaries or through paths within the grains. Subsequent corrosion coupled with a sustained tensile stress acts to initiate a crack. The effect of the tensile stress is in rupturing surface films, thereby exposing fresh metal at the tip of the crack to corrosion reaction. Corrosion pitting is assumed to occur along preferred paths such as slip planes. The electromechanical theory is schematically illustrated in Figure 6 on the following page:

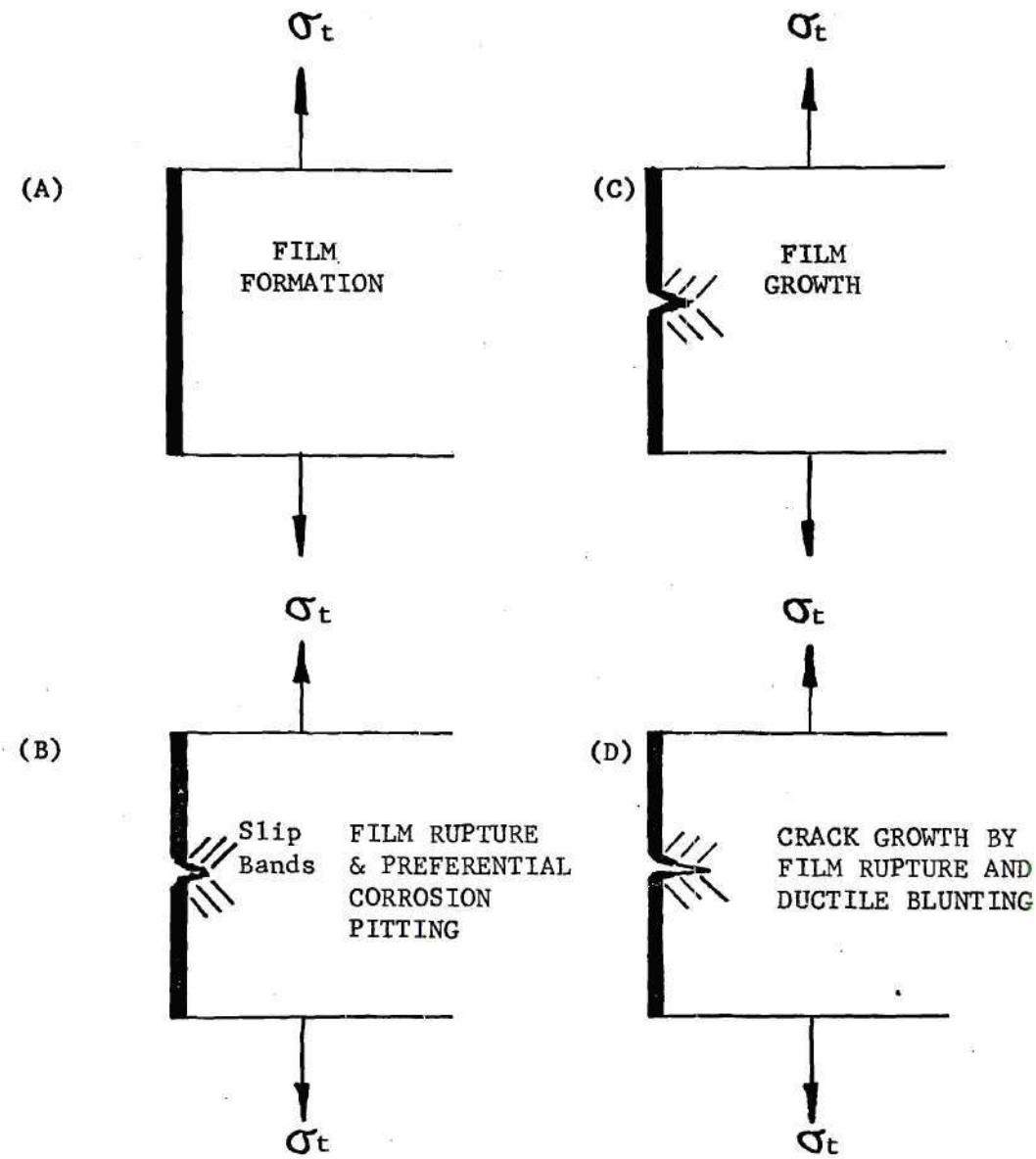

Figure 6. Schematic Illustration of Electrochemical Theory of Stress Corrosion Cracking

The weakness in the electrochemical theory is the lack of a reasonable explanation for stress corrosion cracking in only specific environments, whereas electrochemical reaction would be expected in a variety of related chemical media of comparable conductivity.

Stress Sorption Cracking. The mechanism of stress sorption cracking (12) is based upon crack progression by the weakening of strained metal atomic bonds through absorption of the environments or constituents. The surface energy of the metal is reduced, encouraging the metal to rupture under tensile stress. This mechanism is related to the Griffith criterion of crack formation, which equates elastic strain energy released in the crack extension process in the metal to corresponding increase in surface energy of the crack area (13). Cracking is assumed to become unstable when the incremental release in stored elastic strain energy (dW_e) becomes greater than the incremental increase of surface energy (dW_s)*:

$$dW_e \geq dW_s \tag{1.2}$$

$$W_e = \frac{\pi \sigma^2 c^2}{E} \tag{1.3}$$

$$W_s = 4c\gamma_s \tag{1.4}$$

$$\frac{\partial}{\partial c}\left(\frac{\pi\sigma^2 c^2}{E}\right) \geq \frac{\partial}{\partial c}\left(4c\gamma_s\right) \tag{1.5}$$

*Equation (1.6) is valid for an infinite plate loaded in tension with a crack of length $2c$ and is used here to illustrate the effect of lowering the true surface energy (γ_s) by stress sorption cracking on the critical stress for unstable crack propagation.

$$\sigma_c = \sqrt{\frac{2E\gamma_s}{\pi c}} \tag{1.6}$$

Stress sorption theory accounts for specificity of chemisorption--decrease affinity of surface atoms from themselves or for their environments by formation of a layer of adsorbate specifically chemically bonded to the metal surface--acting to lower the metal surface energy, thus lowering the critical stress for unstable crack growth (σ_c).

The stress sorption theory does not account for the immunity of pure metals to stress corrosion cracking or the importance of lattice structure.

Thesis Problem

A systematic study of the stress corrosion susceptibility of aircraft high-strength aluminum structural components with fastener holes stress coined for fatigue improvement has not been previously investigated. Therefore, the stress distribution resulting from cold working fastener holes by stress coining, and the effect of this deformation on the grain structure is analyzed in this thesis. The objective of this investigation is to relate the effects of stress coining to the structural integrity of the structure when exposed to a corrosive environment. In particular, the problem of susceptibility of AISI 7075-T651 aluminum alloy to stress corrosion cracking has been examined theoretically and experimentally.

CHAPTER II

EXPERIMENTAL PROCEDURES

Alternate Immersion Corrosion Testing

The susceptibility to stress corrosion cracking of stress coined holes was studied using laboratory alternate immersion corrosion testing per ASTM G31-72 (14).

Test Material

A common aircraft aluminum structural material, AISI 7075-T651, was chosen for testing. AISI 7075-T651 is known to be susceptible to stress corrosion cracking when the short transverse grains are continuously stressed as low as seven ksi (15).

The chemical composition in weight per cent was as follows: silicon 0.50; iron 0.7; copper 1.2-2.0; manganese 0.30; magnesium 2.1-2.9; chromium 0.18-0.40; zinc 5.1-6.1; titanium 0.20; other 0.15; and remainder aluminum. The minimum tensile properties listed in the Alcoa Aluminum Handbook (16) for AISI 7075-T651 aluminum two-inch thick plates are given in Table 1:

Table 1. Mechanical Property Limits of Test Specimen Material

Grain Direction	Ultimate Tensile Strength Min. PSI	.2% Offset Yield Strength Min. PSI	Elongation Per cent Min.
Longitudinal	73	65	5
Transverse	73	65	3
Short Transverse	67	63	1

The yield strength of the test specimens was confirmed using Brinell Hardness Testing using a 500-gram load. The average Brinell Hardness obtained was BHN 145. Brinell Hardness number (a pressure in kg/mm^2) for a cold worked metal (no strain hardening) is approximately three times its uniaxial yield strength (17). Therefore, the test specimen average yield strengths were as follows:

$$\sigma_y = \frac{1}{3}\left(145\ kg/mm^2 \times mm^2/.00155\ in^2/.45\ kg\right) = 69{,}200\ psi. \quad (2.1)$$

Test Specimens

Test specimens were machined from plate stock, as shown in Figure 7. Grain orientation was longitudinal, short transverse, as shown. Specimen microstructure is shown in Figure 8.

Five to eight 0.249/0.250-inch holes were drilled in each specimen with hole spacing varying between 1/2-inch and 1-1/4 inches. The hole inside diameters were honed to obtain a $32\sqrt{}$ RMS surface finish.

Six specimens were prepared.

Specimen Stressing

No external load was applied to the test specimens during the test duration. Prior to testing, the holes in five specimens were stress coined by expanding the holes by drawing an oversize cold working mandrel through the holes*. The holes were expanded .006 inch on the diameter (with mandrel inserted), which resulted in an after coining hole size of .253/.254 inch (with mandrel withdrawn). The resultant residual stress

*The test specimens were stress coined using cold working mandrels designed by the author.

distribution is analyzed in Chapter III. One specimen was used as a control, with holes drilled only (no cold working). All specimens were vapor degreased and wiped with acetone-soaked cotton after stressing, and immediately placed in test chamber. The appropriate figures appear on the following pages:

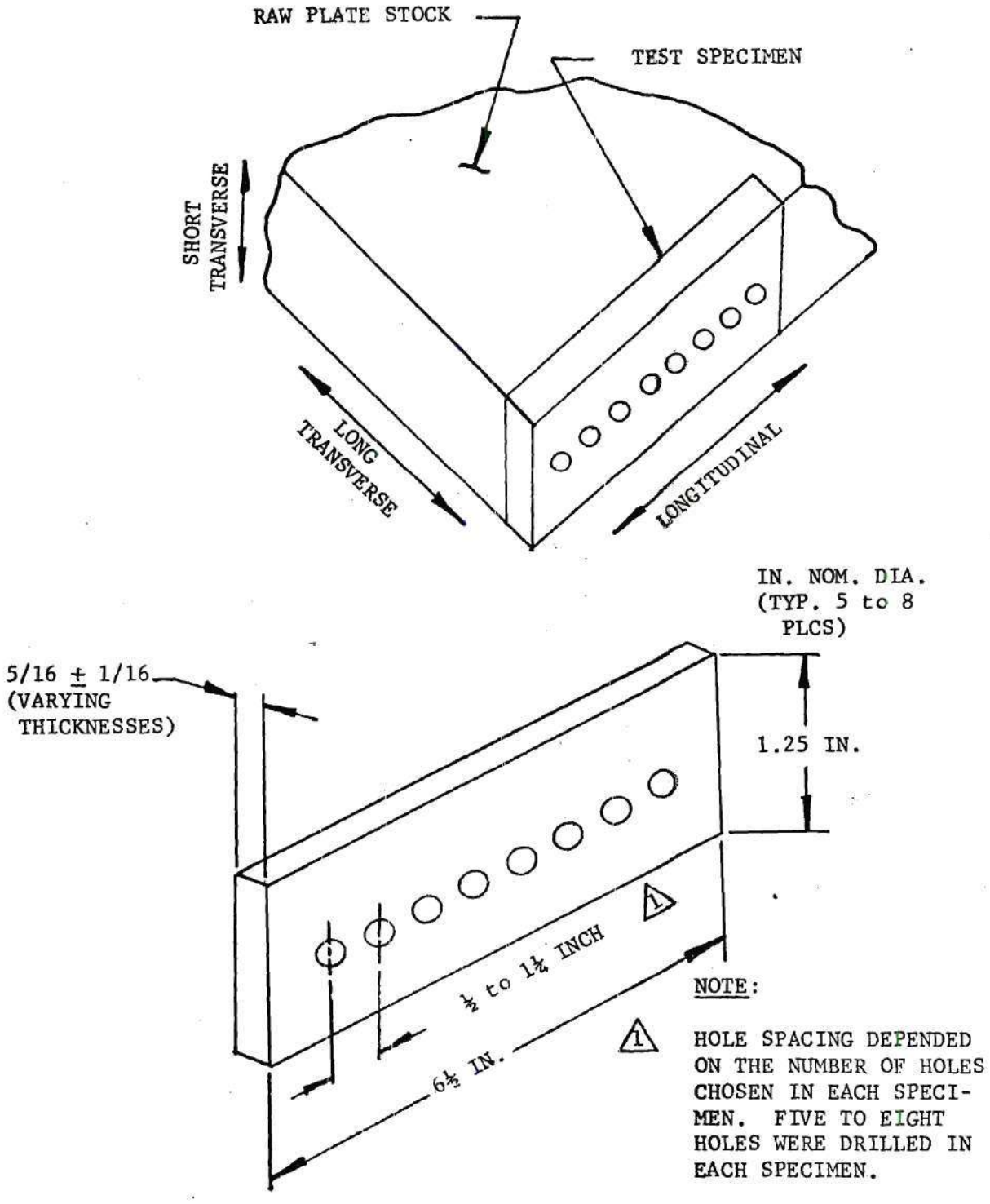

Figure 7. Test Specimen Detail

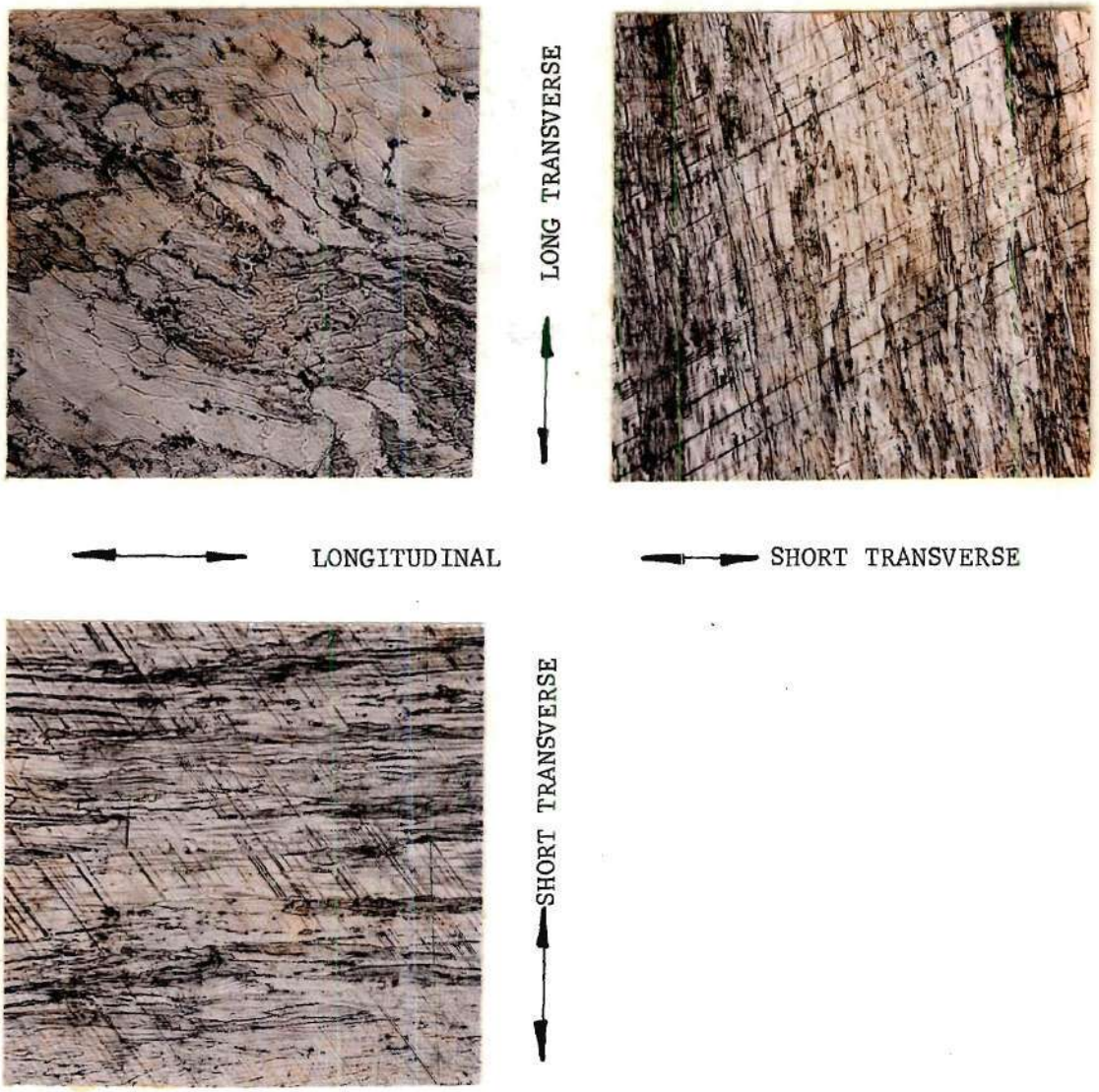

Figure 8. Test Specimen Grain Structure (Magnification 50X)

Test Equipment

A schematic of the equipment is shown in Figure 9. Alternate immersion of the specimens was accomplished by movement of the salt solution. At the beginning of the immersion cycle, the solution was contained in the bottom tank. The cycles were controlled by a timer-actuated solenoid valve which caused air to enter the reservoir tank. The rising pressure caused the salt solution to flow into the test chamber, where the test specimens were suspended. The second timer signal closed the solenoid valve, stopping the flow of air into the tank. The tank pressure then slowly decreased to atmospheric pressure by continual leakage from a bleeder valve, and the salt solution flowed back into the reservoir tank. The cycle was timed for 10 minutes immersion of the test specimens in the salt solution, followed by 50 minutes air-drying time.

Test Medium

The test solution was 3.5 per cent sodium chloride (by weight) and distilled water prepared weekly. The salinity of the solution was checked each day using a hydrometer, and distilled water was added as necessary to compensate for evaporation. Solution Ph was maintained at 6.4-7.2. Air temperature in the test chamber was maintained at 78-82^{o}F., with a relative humidity of 45%. This test solution complies with the test medium requirements of the Federal Test Method Standard No. 151b, Method 823, "Stress Corrosion for Aluminum Alloy Plate, Extrusions, and Forgings by Alternate Immersion." (18). See the following page for the schematic of the test equipment:

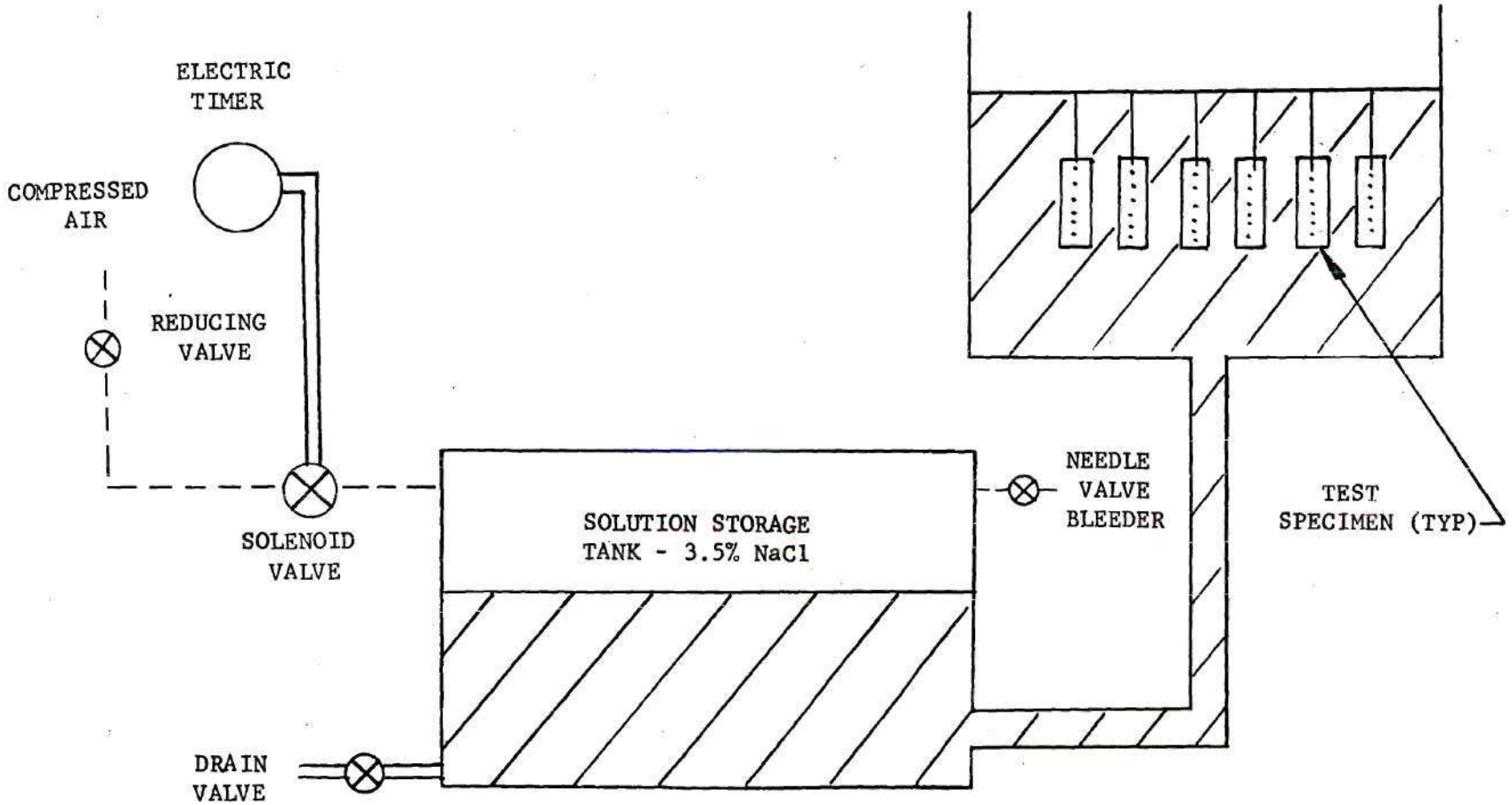

Figure 9. Schematic of Alternate Immersion Corrosion Test Equipment

Test Duration

The stress coined specimens were placed in the alternate immersion corrosion test chamber for 42 days (19). The specimens were visually examined every second day, using a 10X magnifying glass to detect macro-crack initiation. When cracks were detected, the time and location of the crack was recorded, and the specimen was placed back in the test chamber for continuance of the test.

Metallographic Examination

A stress coined and an uncoined test specimen were sectioned perpendicular to the specimen holes, mounted, and metallographically polished, using a magnesium oxide slurry. The specimens were then etched with Kellers Regeant, consisting of 1% HF, 1.5% HCl, 2.5% HNO_3, and 95% distilled water. The cross sections were then examined, using an optical microscope, to compare the microstructure surrounding the coined and uncoined holes. Photomicrographs of the precoined hole and postcoined hole are shown in Figure 10 on the following page. In contrast to the straight and lamellar structure of the uncoined grains, the cold worked grain structure of the stress coined hole exhibited bulging of the grains caused by the local yielding of the hole inside diameter. Severe grain distortion at the edge of the coined hole was detected with the cold working mandrel inserted in the coined hole, as illustrated in Figure 11 on the second page following.

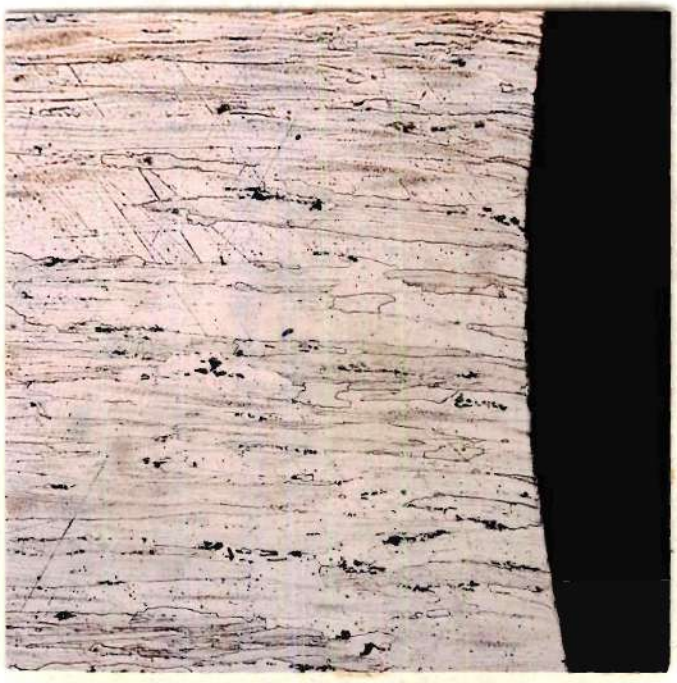

PRECOINED GRAIN STRUCTURE

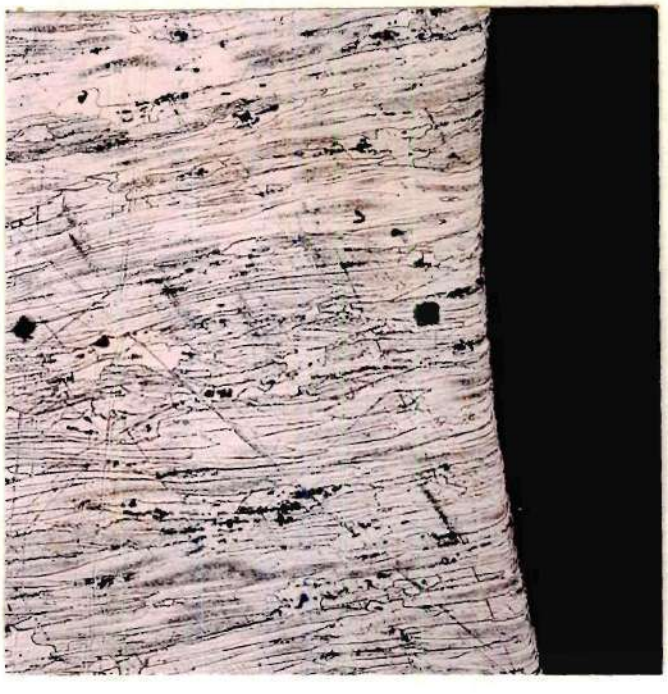

POSTCOINED GRAIN STRUCTURE

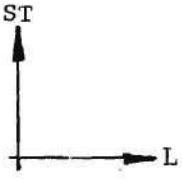

Figure 10. Comparison of Precoined and Postcoined Microstructure (100X)

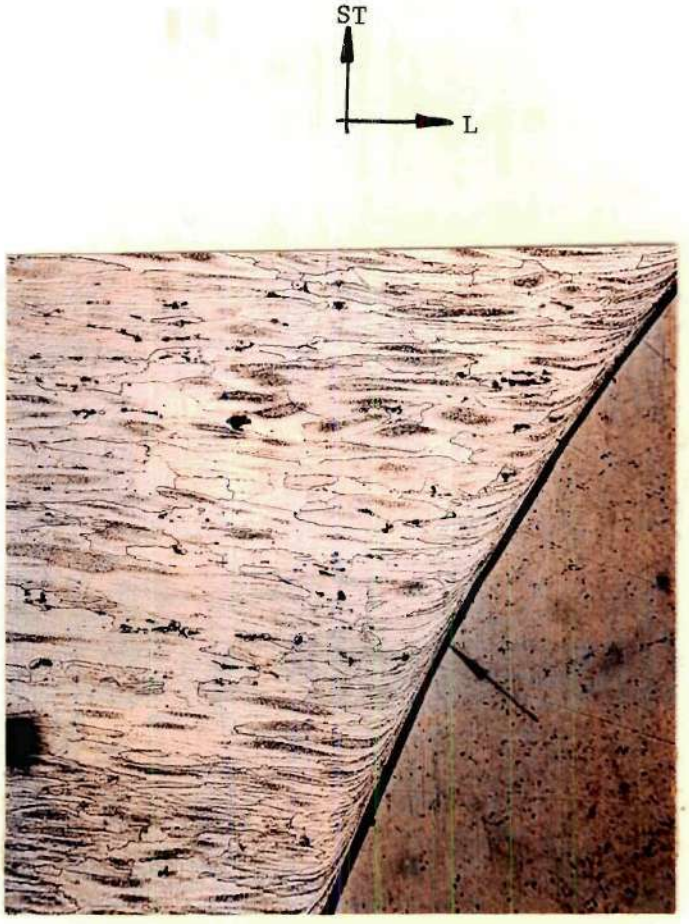

Photomicrograph of cross section perpendicular to stress coined hole with cold working mandrel inserted in fastener hole. Severe grain distoration is visible at the hole-mandrel interface. Etched with Kellers Regeant (100X).

Figure 11. Microstructure During Stress Coining Process

Analysis of Alternate Immersion Test Specimens

Visual Analysis

All the test specimens exhibited corrosion pitting and oxidation by-products on the surfaces of the test specimens. Macrocracking was visible near the holes in two of the five stress coined specimens. The cracking was aligned perpendicular to the specimen short transverse grain direction in each case. The crack sizes varied in length from one-sixteenth inch to one-half inch. The stress coined test specimens with visible cracks are shown in Figures 12 and 22 following on pages 26 and 36, respectively.

The largest crack (see Figure 13, page 27) was broken open for analysis and confirmation of the fracture mode. A well-defined slow growth precracked region was visible, originating symmetrically between two of the stress coined holes and propagating toward the holes. This region had a "flaky" appearance darkened by corrosion products in contrast to the clean and moderately rough texture produced by the opening of the crack after the test for fracture analysis. The precrack had penetrated through approximately 80% of the net section, as shown in Figure 14, page 28.

No visible cracking existed in the uncoined control specimen as shown in Figures 24 and 25, pages 38 and 39, respectively.

Optical Microscopic Examination

The surfaces of the uncoined control specimen and cross sections cut parallel to the short transverse direction were examined microscopically. No microcracking was detected.

The largest crack observed in the stress coined specimen during

the alternate immersion test was sectioned through the crack origin for microscopic examination. The crack originated from the root of a corrosion pit and propagated intergranularly. Multiple secondary intergranular cracking from the corrosion pit was also present. The corrosion attack was preferentially oriented along the grain boundaries. Photomicrographs of the unetched and etched cross section are shown in Figure 15, page 29.

Cross sections cut through the other stress coined test specimens were also examined for microcracking. Multiple intergranular cracking and corrosion pitting was detected on each of the cross sections. Photomicrographs of typical cross sections are shown in Figures 21 and 23, pages 35 and 37, respectively.

Electron Fractography

The crack shown in Figure 13 (page 27) from one of the stress coined specimens (specimen No. 2) was examined using a scanning electron microscope. The electron microscope is used in fracture examination because it offers many advantages over optical microscopy. The unique advantages are depth of field, magnification ranges of 1000X to more than 300,000X, and a high resolving power (20). The high resolution permits observation of fine details on the fracture surface, while the depth of field makes possible the examination of irregularities in the fracture surface that cannot be efficiently examined by optical microscopes. The scanning electron microscope permits direct viewing of the fracture surface. Replication of the fracture surface, as is necessary for viewing with the transmission electron microscope, is not necessary.

The crack origin was scanned to determine the mode of cracking at

the fracture nucleus. The area was covered with corrosion products, with cracks in the corrosion products, giving the surface a typical "mud crack" appearance of stress corrosion cracking as shown in Figure 16. The crack path was intergranular with multiple secondary intergranular cracking illustrated by the photomicrographs shown in Figures 17 and 18. Multiple secondary cracking is typical of stress corrosion cracking and is not usually observed in other types of intergranular cracking (21). The crack transition was characterized by the presence of equiaxed dimples produced by the tensile overstress induced to open the crack for examination, and contrasted vividly with the well-faceted grain structure characteristic of the stress corrosion region as depicted in Figure 19. Figures 16, 17, 18 and 19 are shown on the following pages:

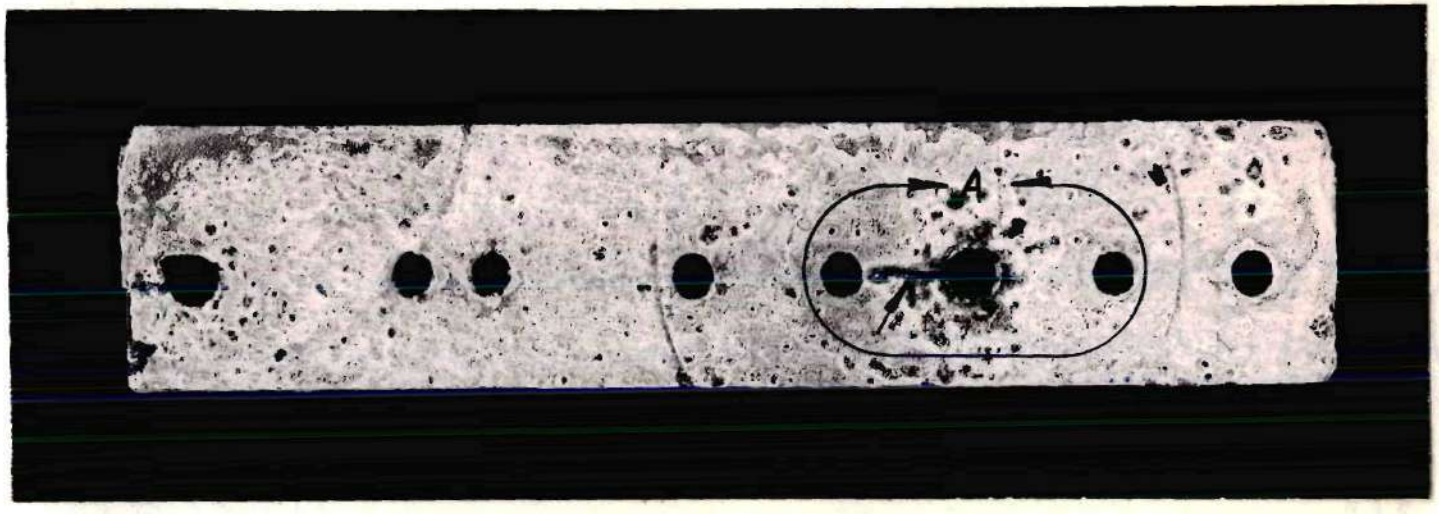

Detail of stress coined specimen No. 2 showing macrocracking (indicated by arrows) in the vicinity of three of the cold worked holes. Cracking was first visually detected after 28 days alternate immersion 3.5% NaCl exposure. The entire test specimen surface is covered with corrosion products.

Figure 12. Plan View of Test Specimen No. 2 (Magnification 0.98X)

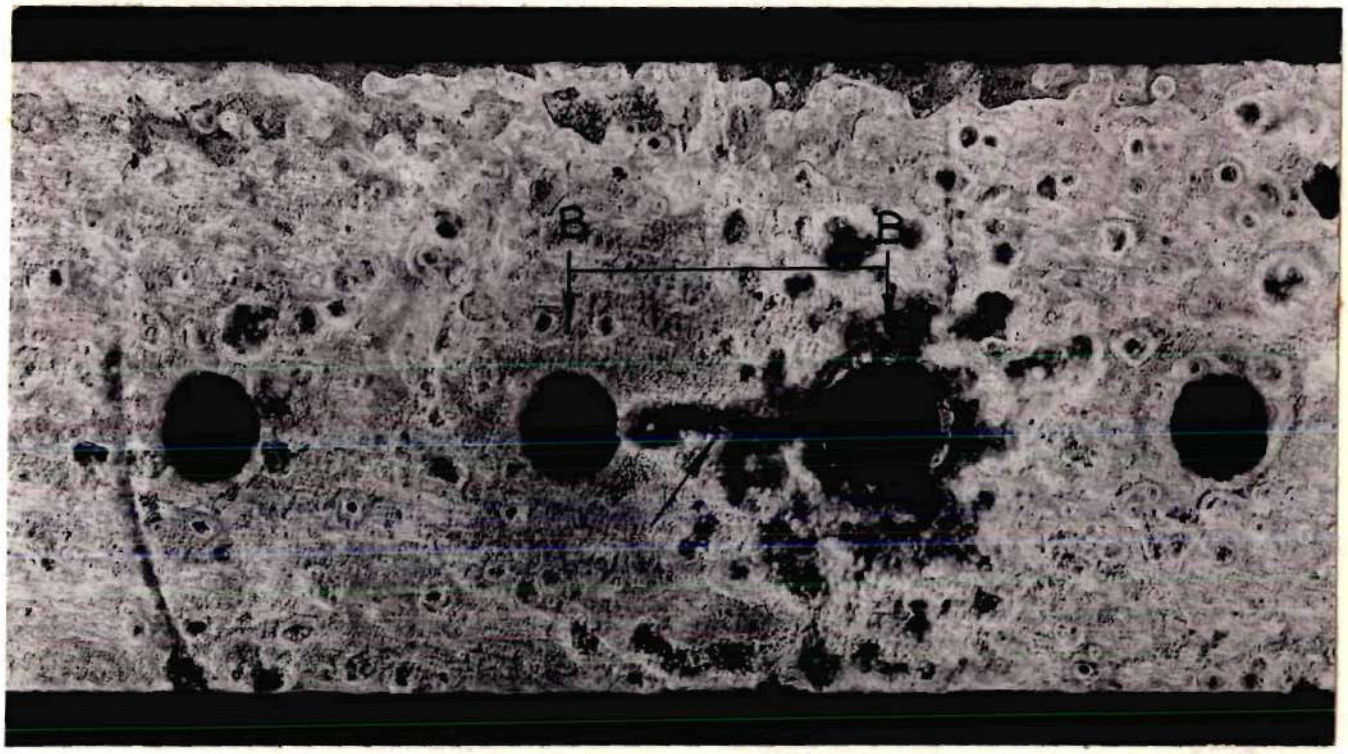

Detail A (Ref. Figure 12). Shown is the largest crack that appeared during the alternate immersion corrosion test. The crack extended between two of the stress coined holes and was aligned with the specimen longitudinal grain direction. Corrosion pitting is visible on the specimen surface. Section B-B is shown in Figure 14.

Figure 13. Detail of Macrocracking in Stress Coined Test Specimen (Magnification 2.0X)

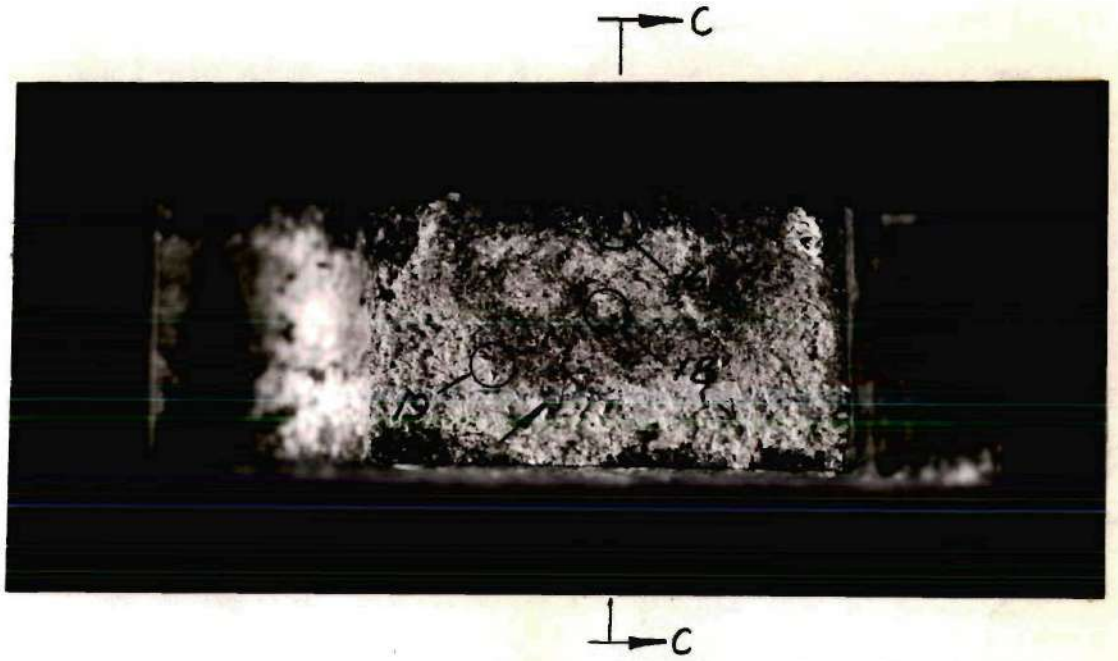

Shown above is the fracture surface after breaking open the crack shown in Figure 13, Section B-B. The slow growth region can be distinguished from the rapid fracture area (indicated by arrow). Cross Section C-C is shown in Figure 15. Highlighted areas refer to Figure Nos. depicting areas examined by electron fractography.

Figure 14. Photomacrograph of Largest Crack Fracture Surface in Specimen No. 2 (Magnification 5.0X)

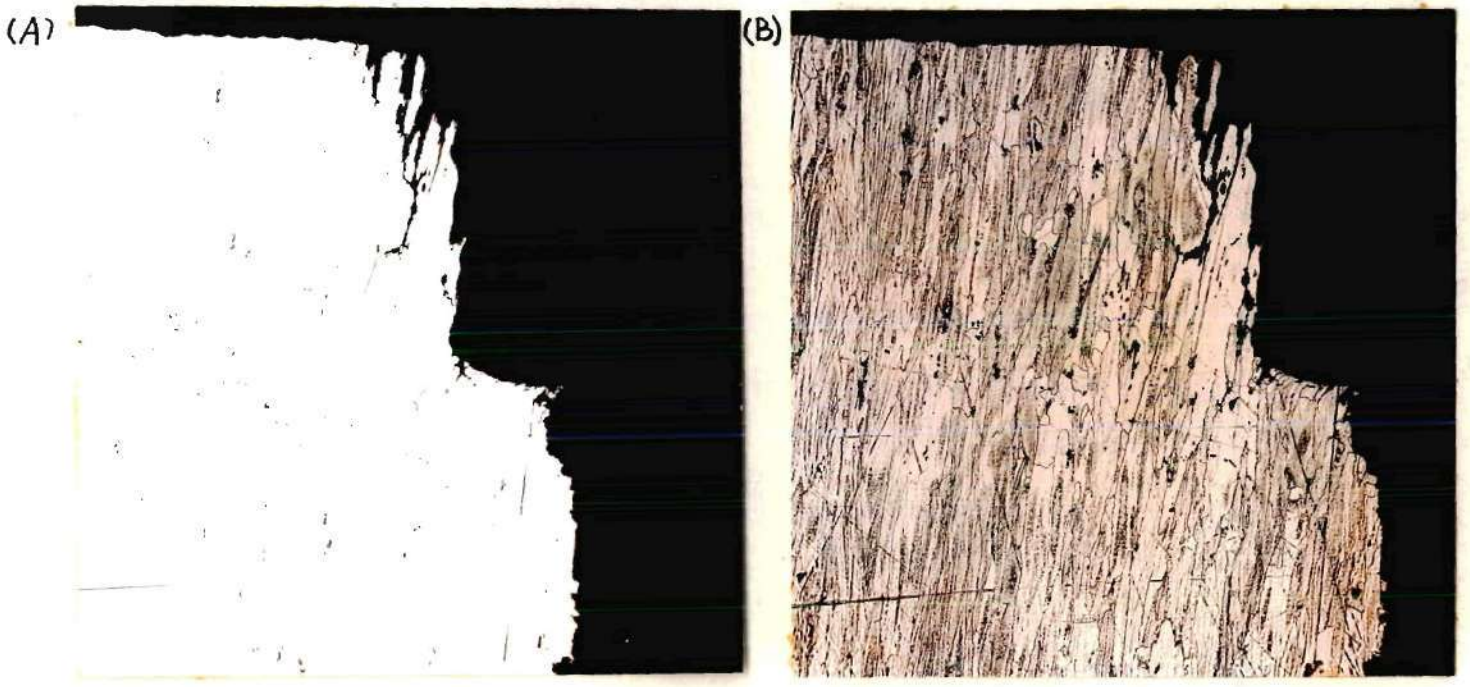

Shown above are photomicrographs of cross section cut through the crack (Ref. Figure 14, Section C-C) indicating preferentially oriented corrosion pitting at the crack initiation and auxiliary intergranular cracking. Cross section (A) was metallographically polished only; cross section (B) was etched with Kellers Regeant.

Figure 15. Details of Cross Section Through Crack Origin (Magnification 100X)

Scanning electron fractograph of crack origin. Fracture surface shows "mud crack" appearance typical of stress corrosion cracking in aluminum alloys. Fracture surface is covered with corrosion products. Multiple intergranular secondary cracking is present.

Figure 16. Electron Fractography (Magnification 2000X)

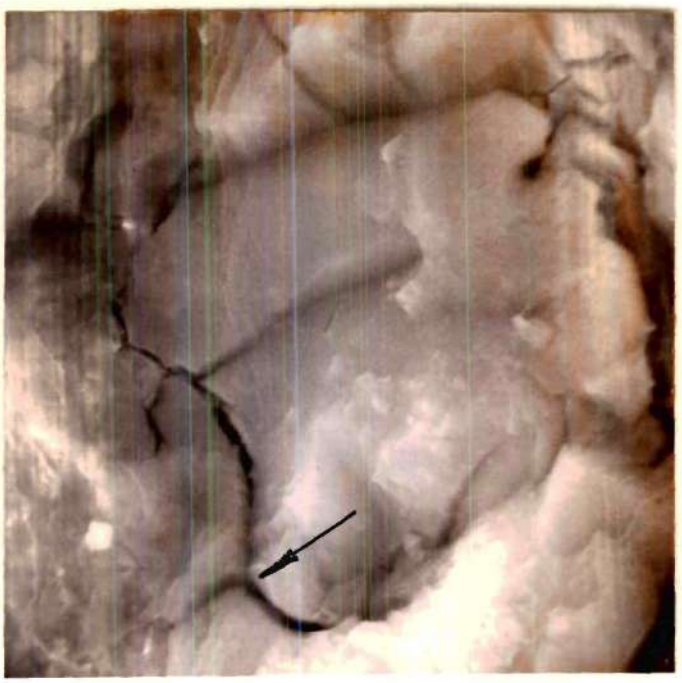

Higher magnification fractograph depicting the secondary intergranular cracking and corrosion products on the fracture surface in the crack origin region.

Figure 17. Electron Fractography (Magnification 6000X)

Scanning electron fractograph of area approximately one-eighth inch from fracture origin (see Figure 14). Large grain boundary separation is present, typical of stress corrosion cracking.

Figure 18. Electron Fractography (Magnification 5500X)

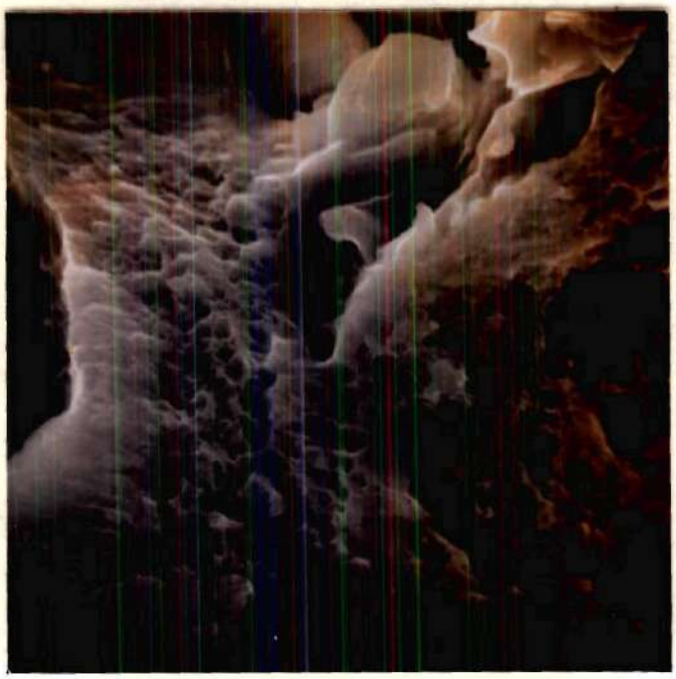

Scanning electron photomicrograph of crack transition area at crack tip. Fracture mode is microvoid coalescence due to overstress during breaking open of the crack for examination. The equiaxed dimples characteristic of the overload fracture contrast to the prior intergranular stress corrosion cracking in upper portion of the fractograph.

Figure 19. Electron Fractography (Magnification 5000X)

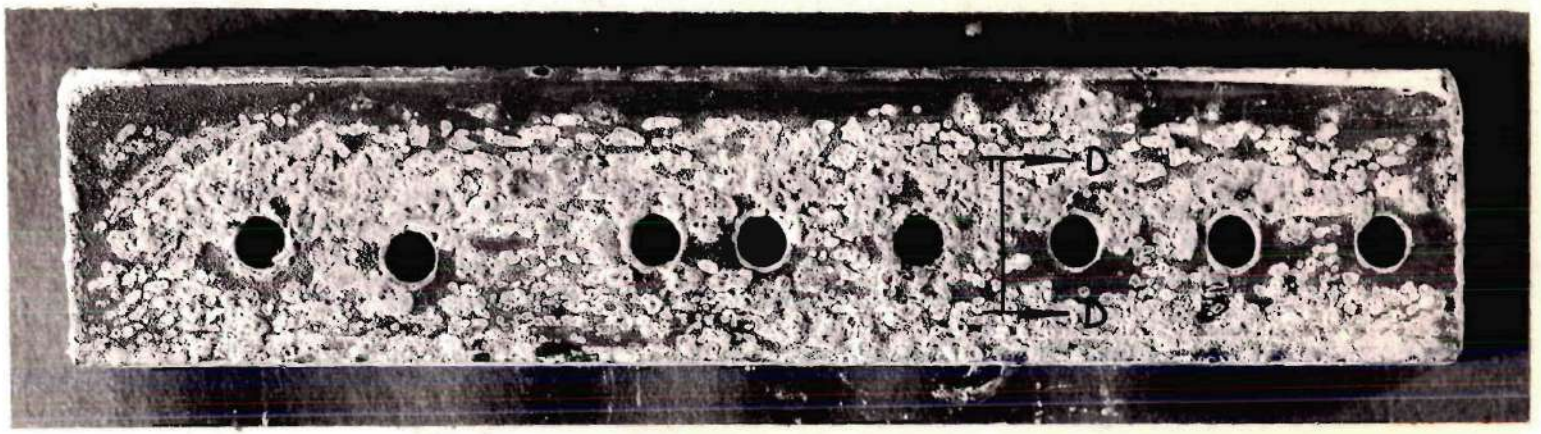

Detail of stress coined specimen No. 3 showing no visible macrocracking after 42 days alternate immersion 3.5% NaCl exposure. Specimen was sectioned as shown in Section D-D and metallographically polished for examination using optical microscopy (see Figure 21). Test specimen surface is covered with corrosion products.

Figure 20. Plan View of Test Specimen No. 3 (Magnification 1.1X)

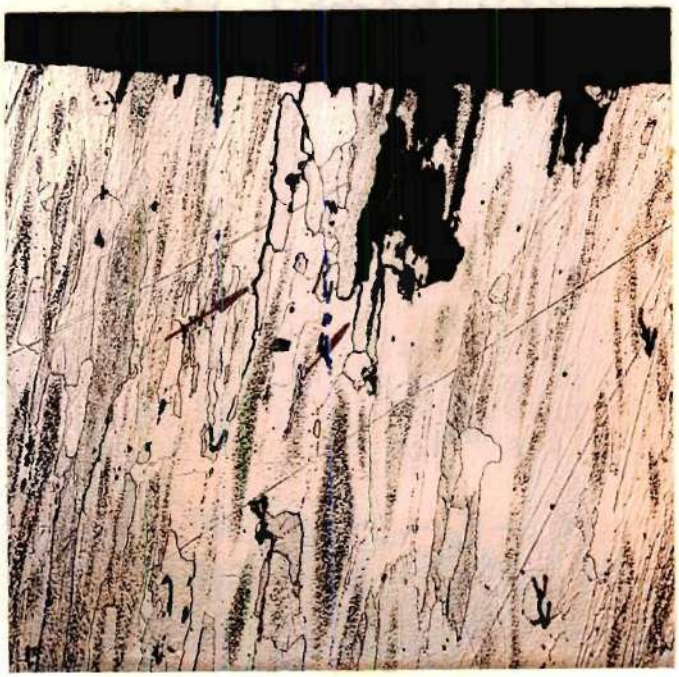

Examination of cross section D-D (Ref. Figure 20) showed preferential corrosion pitting along grain boundaries on the specimen surface with multiple intergranular micro-cracking present. Cross section was etched with Kellers Etch.

Figure 21. Cross Section Through Test Specimen No. 3 (Magnification 200X)

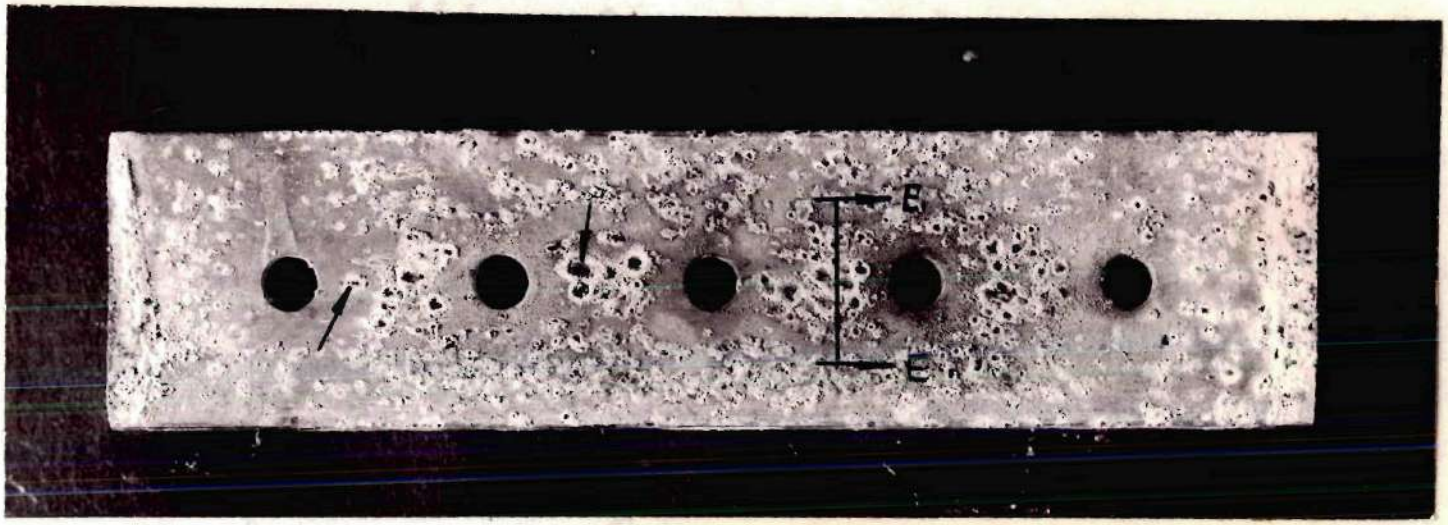

Detail of stress coined specimen No. 4 showing visible macrocracking around the cold worked holes. Cracking was first visually detected after 35 days of alternate immersion 3.5% NaCl exposure. The test specimen was sectioned as shown in Section E-E and examined using optical microscopy after completion of corrosion test (see Figure 23).

Figure 22. Plan View of Test Specimen No. 4 (Magnification 0.98X)

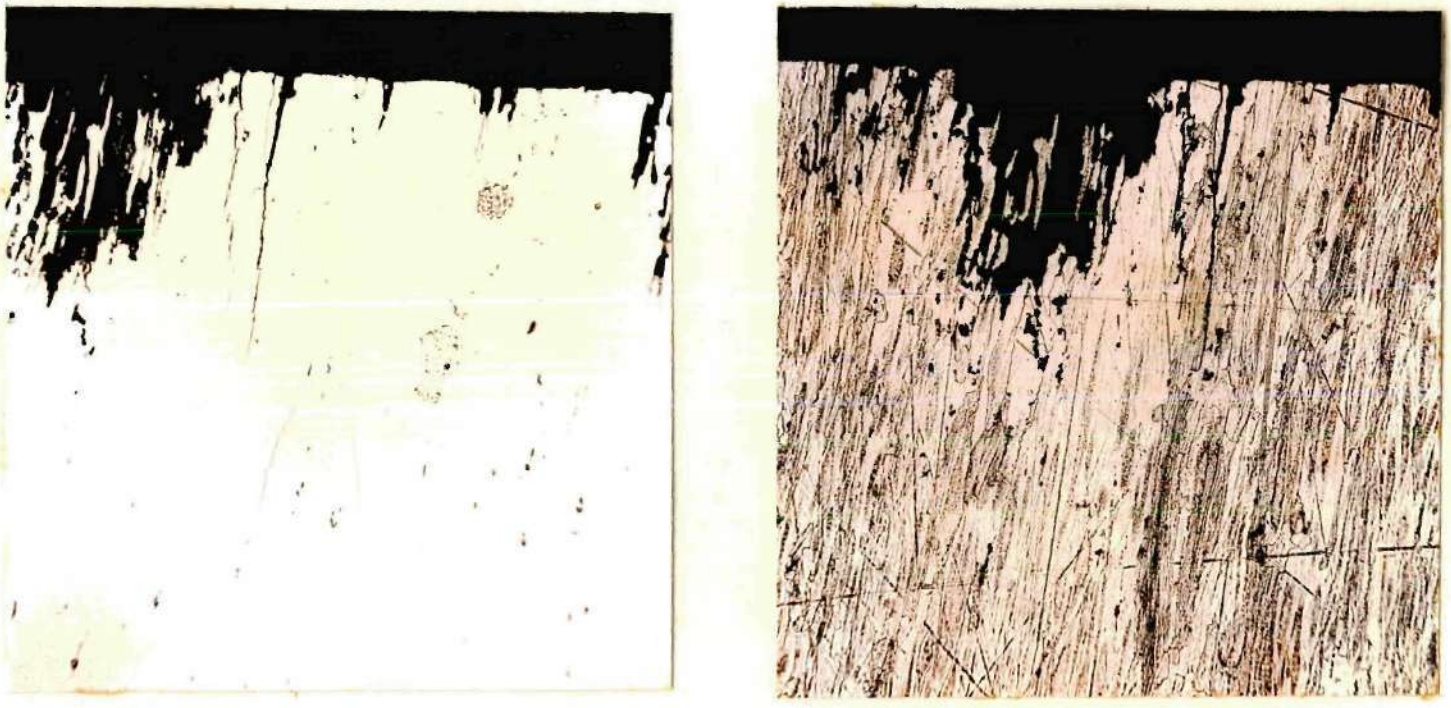

Details above depict etched and unetched cross section E-E (see Figure 22) showing severe corrosion pitting and intergranular cracking. Cross section was etched with Kellers Etch.

Figure 23. Cross Section Through Test Specimen No. 4 (Magnification 100X)

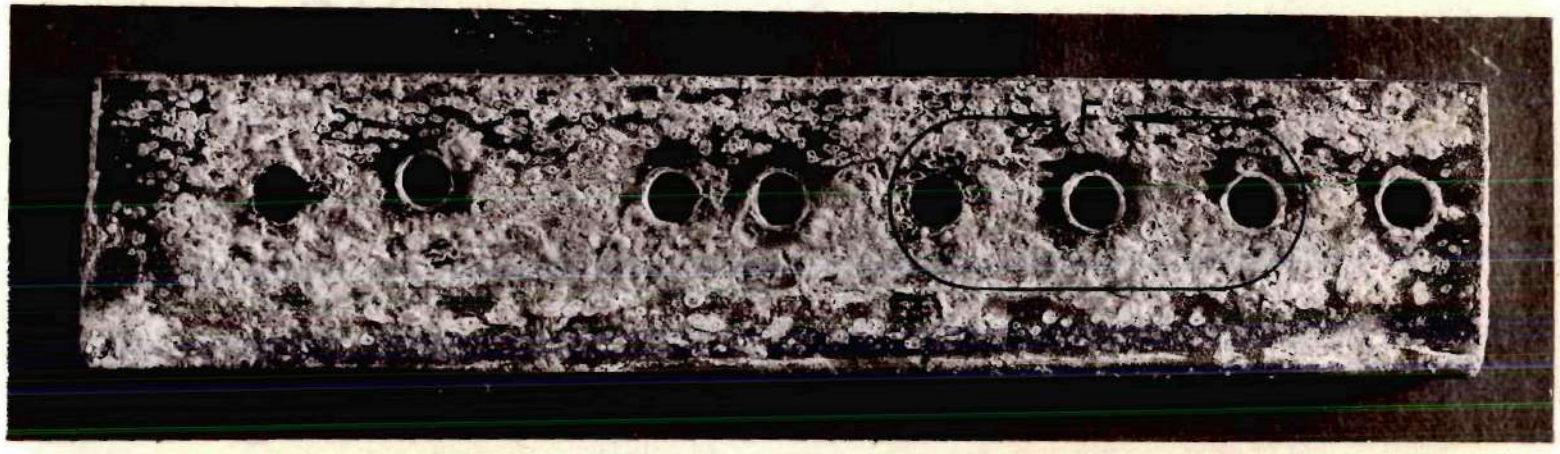

Detail of uncoined control specimen. No visible macrocracking occurred on test specimen after 42 days alternate immersion 3.5% NaCl exposure. The specimen surface is covered with corrosion products. Detail F is shown in Figure 25.

Figure 24. Plan View of Control Specimen (Magnification 1.1X)

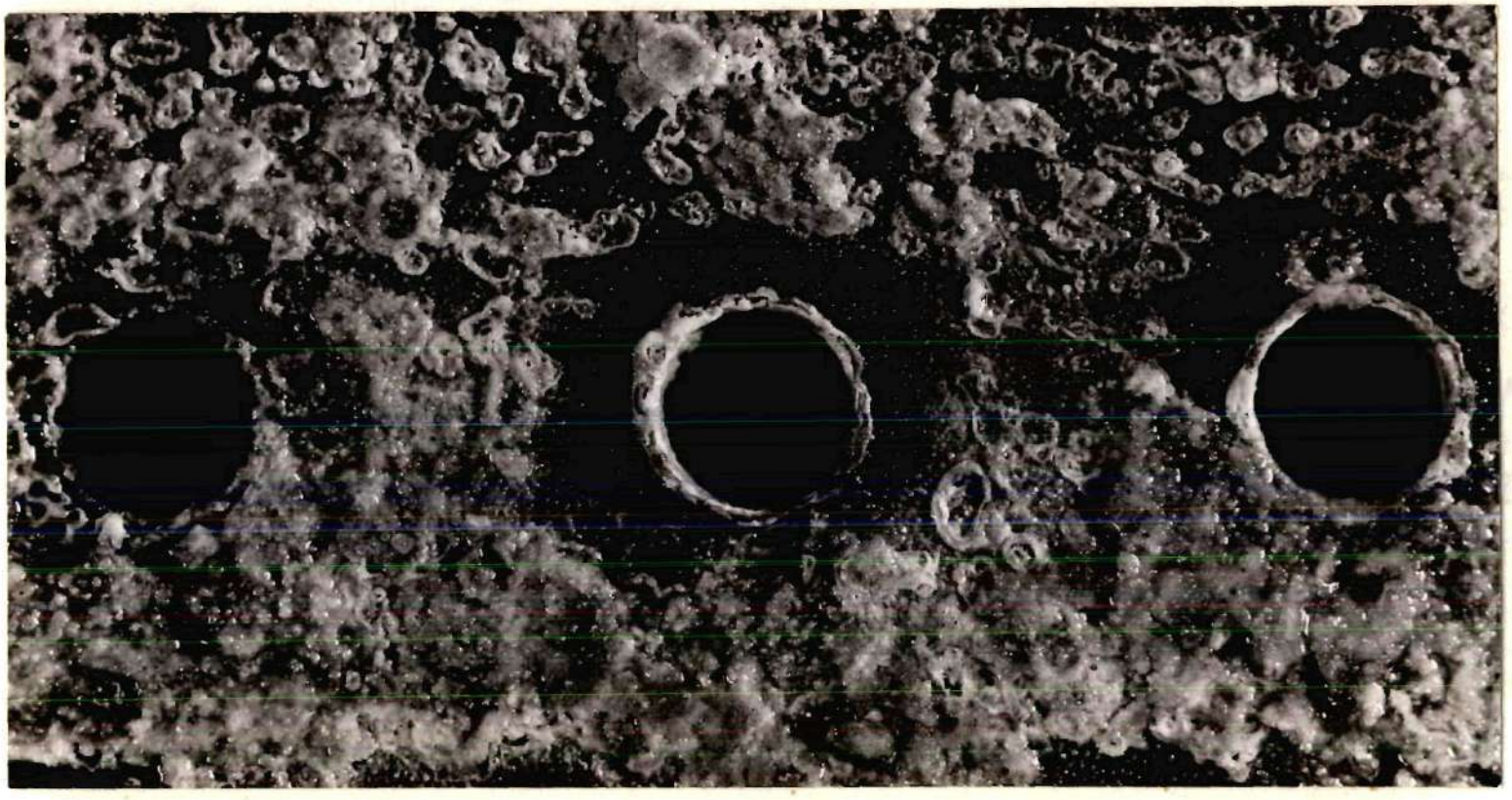

Higher magnification of region surrounding typical holes (Detail F, see Figure 24) showing absence of cracking after duration of alternate immersion corrosion test.

Figure 25. Detail of Typical Region Surrounding Holes in Uncoined Specimen (Magnification 5X)

CHAPTER III

ANALYTICAL DEVELOPMENT

The stress distribution resulting from the stress coining process used for fatigue improvement of fastener holes in aircraft structures is analyzed in the Appendix to relate the resulting residual stresses to the stress corrosion threshold stress of the cold worked material. The problem is first analyzed by assuming that the deformation was all elastic to determine the limiting elastic radial boundary displacement upon the onset of yielding. The parameters for this condition are shown in Figure 27 of the Appendix. The problem is then examined by assuming elastic-plastic deformations during the loading cycle, i.e., inserting the cold working mandrel into the hole as schematically illustrated in Figure 28 of the Appendix. After obtaining the resulting stress and displacement distribution during loading, the residual stresses are then obtained by assuming completely elastic unloading while withdrawing the cold working mandrel from the coined hole.

The analysis is based upon the following assumptions:

(1) Hooke's Law is valid in the elastic zone

(2) Plane stress conditions are prevalent during deformation

(3) All displacements are small

(4) The cold worked material is isotropic and ideally plastic (no strain hardening)

(5) Tresca or maximum shear stress failure criteria is used to predict yielding

(6) Deformation in the plastic zone is of the "incremental" type

(7) Fastener holes are "sufficiently spaced" such that no interaction of the deformation occurs

(8) The cold working mandrel is a rigid body

(9) Thickness variations in the plastic region are neglected.

The resulting residual stress distribution obtained in the analysis is as follows:

$$\sigma_{r_{Residual}} = \begin{cases} \frac{\sigma_Y}{2}\left(\frac{a^2}{r^2}-1\right) + \sigma_y \ln\frac{r}{b} - \frac{\sigma_Y a^2}{r^2}\ln\frac{a}{b} & \text{for } a \le r \le b \\ -\frac{\sigma_Y b^2}{2r^2} - \frac{\sigma_Y a^2}{r^2}\ln\frac{a}{b} + \frac{\sigma_Y a^2}{2r^2} & \text{for } b \le r \end{cases} \quad (3.1)$$

$$\sigma_{\theta_{Residual}} = \begin{cases} \frac{\sigma_Y}{2}\left(1-\frac{a^2}{r^2}\right) + \sigma_y \ln\frac{r}{b} + \frac{\sigma_Y a^2}{r^2}\ln\frac{a}{b} & \text{for } a \le r \le b \\ \frac{\sigma_Y b^2}{2r^2} + \sigma_Y \frac{a^2}{r^2}\ln\frac{a}{b} - \frac{\sigma_Y a^2}{2r^2} & \text{for } b \le r \end{cases} \quad (3.2)$$

The derivation of these equations can be seen in the Appendix. A graph depicting this stress distribution is shown in Figure 26, page 42. As can be seen, the maximum tensile residual stress occurs at r = b, i.e., at the elastic-plastic boundary.

For the stress corrosion alternate immersion test specimens examined in Chapter II and made from AISI 7075-T651 aluminum alloy, the controlling parameters are:

$a = 0.125$ inch $\qquad \nu = 0.32$

$\sigma_y = 65{,}000$ psi $\qquad \frac{b}{a} = 2.5$

$E = 10{,}300{,}000$ psi

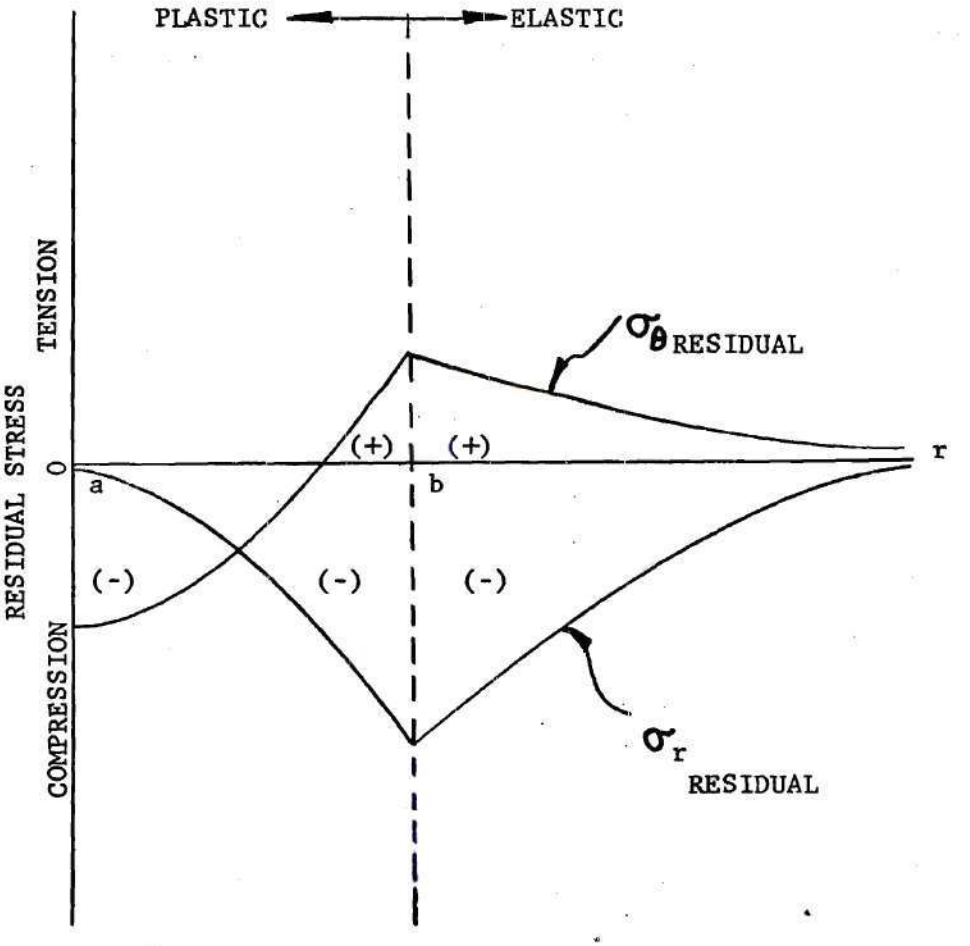

NOTE: a ~ EXPANDED HOLE RADIUS
b ~ ELASTIC-PLASTIC BOUNDARY
r ~ RADIAL DISTANCE

Figure 26. Residual Stress Distribution Produced by Cold Working Holes by the Stress Coining Process

For this case, the maximum tensile residual stress is 18,400 psi, occuring 0.312 inch from the hole centers. This sustained stress is greater than the stress corrosion threshold stress of seven ksi (22) for the material tested.

CHAPTER IV

RESULTS AND CONCLUSIONS

The analytical development outlined in Chapter III and derived in the Appendix shows that the short transverse stress corrosion threshold level in AISI 7075-T651 aluminum alloy is exceeded by the expansion of fastener holes by stress coining.

The maximum residual tensile stress caused by the cold working occurs at the elastic-plastic boundary as shown theoretically in Chapter III. The location of the maximum tensile stress is also confirmed experimentally in Chapter II by the position of the crack origins in the alternate immersion corrosion test specimens.

Stress corrosion cracking may occur resulting from the sustained stresses produced by the stress coining process without the application of any other externally applied loads. This has been demonstrated in Chapter II by alternate immersion stress corrosion testing, with the mode of cracking confirmed by examination of the crack surfaces by electron fractography.

CHAPTER V

RECOMMENDATIONS

The thesis study of the stress corrosion susceptibility of stress coined fastener holes has led the author to other suggested allied problems for future research. These include:

(1) The study of the stress corrosion susceptibility of stress coined fastener holes in other commonly used aircraft structural materials.

(2) The study of the effect of other methods of fatigue improvement such as interference fit fasteners and "pressed in" bushings on the stress corrosion susceptibility of commonly used aircraft materials.

(3) The study of stress corrosion growth rates of cracks from stress coined fastener holes and the instrumentation necessary to accomplish this study.

(4) The application of fracture mechanics to the stress corrosion cracking problem.

APPENDIX

APPENDIX

Stress distribution resulting from the stress coining process used for fatigue improvement of fastener holes in aircraft structures is analyzed to relate the resulting residual stresses to the stress corrosion threshold stress of the cold worked material. The problem is first analyzed by assuming that the deformation was all elastic to determine the limiting elastic radial boundary displacement upon the onset of yielding. The problem is then examined by assuming elastic-plastic deformation during the loading cycle, i.e., inserting the cold working mandrel into the hole. After obtaining the resulting stress and displacement distribution during loading, the residual stresses are then obtained by assuming completely elastic unloading while withdrawing the cold working mandrel from the coined hole.

The analysis is based upon the following assumptions:

(1) Hooke's Law is valid in the elastic zone.

(2) Plane stress conditions are prevalent during deformation.

(3) All displacements are small.

(4) The cold worked material is isotropic and ideally plastic (no strain hardening).

(5) Tresca or maximum shear stress failure criteria is used to predict yielding.

(6) Deformation in the plastic zone is of the "incremental" type.

(7) Fastener holes are "sufficiently spaced" such that no interaction of the deformation occurs.

(8) The cold working mandrel is a rigid body.

(9) Thickness variations in the plastic region are neglected.

Elastic Analysis

For the elastic analysis, a stress coined fastener hole with the cold working mandrel inserted into the hole is represented by the parameters shown in Figure 27. From the condition of radial symmetry, it follows that there are no shearing stresses produced on the element "defg" shown in Figure 27. Then the equilibrium equation (neglecting the weight of the element) in polar coordinates is:

$$\sigma_\theta - \sigma_r - r\frac{d\sigma_r}{dr} = 0 \tag{A.1}$$

All points in the deformed region around the stress coined hole are displaced radially only by the assumption of radial symmetry. Thus, the displacement varies along the radial direction "r" only. If "u" denotes the radial displacement of a cylindrical surface of radius "r" around the cold worked hole, then the strain-displacement relations for the unit elongation on the element "defg" are:

$$\epsilon_r = \frac{du}{dr} \tag{A.2}$$

$$\epsilon_\theta = \frac{u}{r} \tag{A.3}$$

$$\epsilon_z = \frac{dw}{dz} \tag{A.4}$$

$$\gamma_{r\theta} = \gamma_{\theta z} = \gamma_{rz} = 0 \tag{A.5}$$

(A) STRESS COINED HOLE WITH THE COLD WORKING MANDREL INSERTED:

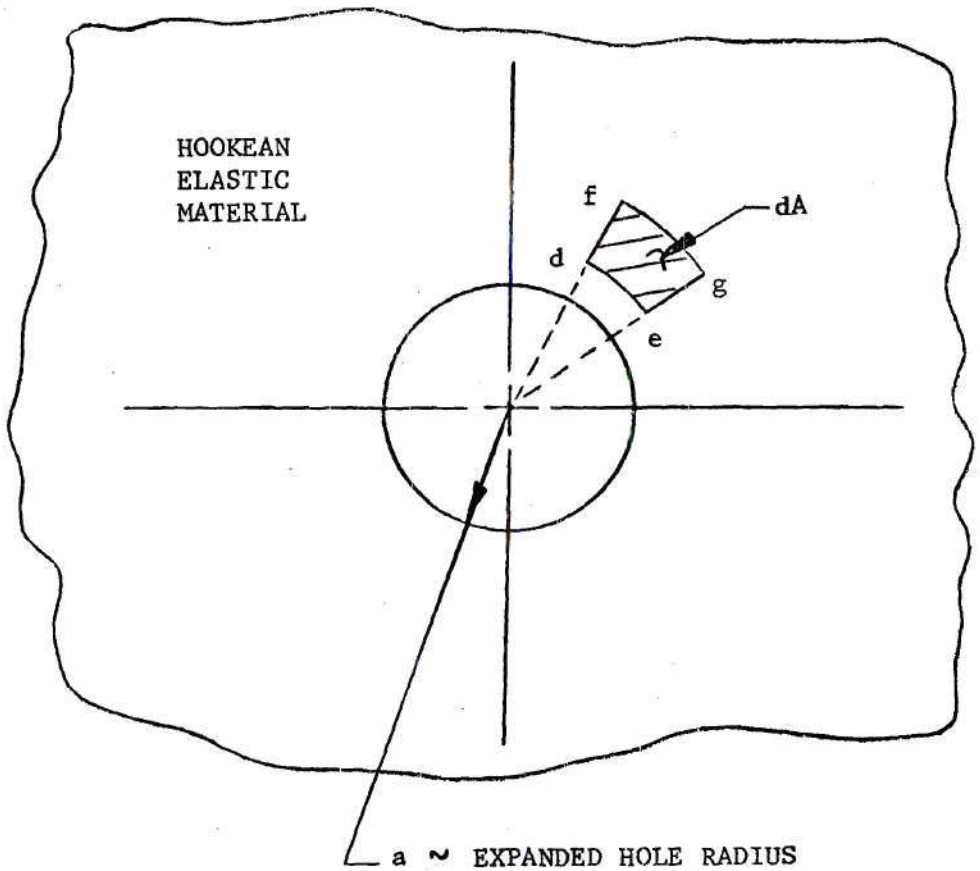

(B) DETAIL OF ELEMENT dA:

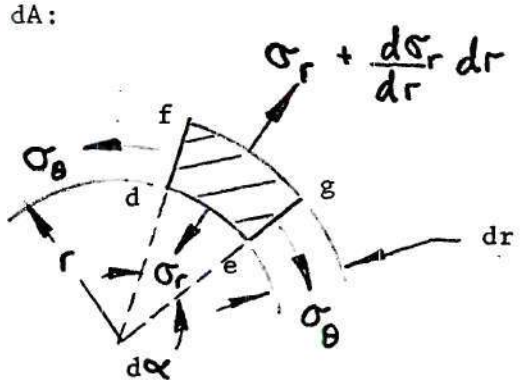

Figure 27. Schematic of Stress Coined Fastener Hole for Elastic Analysis

Hooke's Law for relating the elastic stresses and strains caused by the deformation gives the following equations:

$$\epsilon_r = \frac{\sigma_r}{E} - \frac{\nu}{E}\sigma_\theta \tag{A.6}$$

$$\epsilon_\theta = \frac{\sigma_\theta}{E} - \frac{\nu}{E}\sigma_r \tag{A.7}$$

$$\epsilon_z = -\frac{\nu}{E}(\sigma_r + \sigma_\theta) \tag{A.8}$$

Combining Hooke's law and the strain-displacement equations yields the following relations:

$$\frac{du}{dr} = \frac{1}{E}(\sigma_r - \nu\sigma_\theta) \tag{A.9}$$

$$\frac{u}{r} = \frac{1}{E}(\sigma_\theta - \nu\sigma_r) \tag{A.10}$$

$$\frac{dw}{dz} = -\frac{\nu}{E}(\sigma_r + \sigma_\theta) \tag{A.11}$$

which can be solved simultaneously for σ_r and σ_θ yielding

$$\sigma_r = \frac{E}{1-\nu^2}\left(\frac{du}{dr} + \nu\frac{u}{r}\right) \tag{A.12}$$

$$\sigma_\theta = \frac{E}{1-\nu^2}\left(\frac{u}{r} + \nu\frac{du}{dr}\right) \tag{A.13}$$

Substitution of these equations (A.12) and (A.13) into the equilib-

rium equation (A.1) gives the governing differential equation for the elastic problem:

$$\frac{d^2u}{dr^2} + \frac{1}{r}\frac{du}{dr} - \frac{u}{r^2} = 0 \qquad (A.14)$$

The general solution of this equation is:

$$u = C_1 r + \frac{C_2}{r} \qquad (A.15)$$

Substitution of the general solution for displacement (A.15) into the expressions for σ_r and σ_θ (A.12 and A.13) gives:

$$\sigma_r = \frac{E}{1-\nu^2}\left\{C_1(1+\nu) - \frac{C_2}{r^2}(1-\nu)\right\} \qquad (A.16)$$

$$\sigma_\theta = \frac{E}{1-\nu^2}\left\{C_1(1+\nu) + \frac{C_2}{r^2}(1-\nu)\right\} \qquad (A.17)$$

The constants C_1 and C_2 are determined by the boundary conditions known at r = a and r = ∞ . At r = a, the radial displacement (u) is known since the cold working mandrel is assumed to be rigid. At r = ∞ , the elastic zone size radius, the radial stress σ_r becomes zero. Therefore, using these conditions yields:

$$\lim_{r\to\infty} \sigma_r(r) = 0 \qquad (A.18)$$

$$\lim_{r\to\infty} \frac{E}{1-\nu^2}\left\{C_1(1+\nu) - \frac{C_2}{r^2}(1-\nu)\right\} = 0 \tag{A.19}$$

$$\therefore \quad \frac{C_1 E}{1-\nu} = 0 \tag{A.20}$$

$$C_1 = 0 \tag{A.21}$$

and $$u(a) = C_1 a + \frac{C_2}{a} = u_o \tag{A.22}$$

$$C_2 = a u_o \tag{A.23}$$

Substitution of the values for constants C_1 and C_2 into the equations for u, σ_r and σ_θ gives

$$u = \frac{a u_o}{r} \tag{A.24}$$

$$\sigma_r = -\frac{E}{1+\nu}\left(\frac{a u_o}{r^2}\right) \tag{A.25}$$

$$\sigma_\theta = \frac{E}{1+\nu}\left(\frac{a u_o}{r^2}\right) \tag{A.26}$$

$$\left|\sigma_\theta - \sigma_r\right| = \frac{2E}{1+\nu}\left(\frac{a u_o}{r^2}\right) \tag{A.27}$$

The maximum value of $\left|\sigma_\theta - \sigma_r\right|$ occurs at r = a. Substitution of r = a in equation (A.27) gives:

$$\left|\sigma_\theta - \sigma_r\right|_{MAX.} = \frac{2E}{1+\nu}\left(\frac{u_o}{a}\right) \tag{A.28}$$

Using Tresca Maximum Shear failure criterion for yielding

$$\left|\sigma_\theta - \sigma_r\right| = \sigma_y \tag{A.29}$$

gives the limiting elastic boundary displacement (u_{oe}):

$$u_{oe} = \frac{\sigma_y (1+\nu)\, a}{2E} \tag{A.30}$$

For the stress coined test specimens examined in Chapter II machined from AISI 7075-T651 aluminum, the controlling parameters were:

$a = 0.125$ inch

$\sigma_y = 65{,}000$ psi

$E = 10{,}300{,}000$ psi

$\nu = 0.32$

Substitution of these values into equation (A.30) gives:

$$u_{oe} = \frac{(6.5 \times 10^4)\ (1.32)\ (0.125)}{20.6 \times 10^6} \tag{A.31}$$

$$u_{oe} = .0005 \text{ inch} \tag{A.32}$$

The limiting elastic boundary displacement u_{oe} was necessary to obtain for use in the elastic-plastic analysis, which follows.

Elastic-Plastic Analysis

Loading

For the elastic-plastic analysis, deformation zones are shown

schematically in Figure 28 for the loading cycle. Two deformation zones are now present with the deformed material ideally plastic in the zone $a \leq r \leq b$ and Hookean elastic material in the region $b \leq r$. The equilibrium conditions for the two zones are:

$$\sigma_{\theta_p} - \sigma_{r_p} - r\frac{d\sigma_{r_p}}{dr} = 0 \quad \text{for} \quad a \leq r \leq b \tag{A.33}$$

$$\sigma_{\theta_e} - \sigma_{r_e} - r\frac{d\sigma_{r_e}}{dr} = 0 \quad \text{for} \quad b \leq r \tag{A.34}$$

From the elastic analysis, the radial and tangential stresses, and displacement for the region $r \geq b$ can be written as follows:

$$u_e = C_3 r + \frac{C_4}{r} \tag{A.35}$$

$$\sigma_{r_e} = \frac{E}{1-\nu^2}\left\{C_3(1+\nu) - \frac{C_4}{r^2}(1-\nu)\right\} \tag{A.36}$$

$$\sigma_{\theta_e} = \frac{E}{1-\nu^2}\left\{C_3(1+\nu) + \frac{C_4}{r^2}(1-\nu)\right\} \tag{A.37}$$

At this point, it is convenient to use the boundary condition at $r = \infty$ to simplify the expressions for σ_{r_e} and σ_{θ_e}. At $r = \infty$, the elastic radial stress (σ_{r_e}) vanishes. Therefore,

$$\lim_{r \to \infty} \sigma_r(r) = 0 \tag{A.38}$$

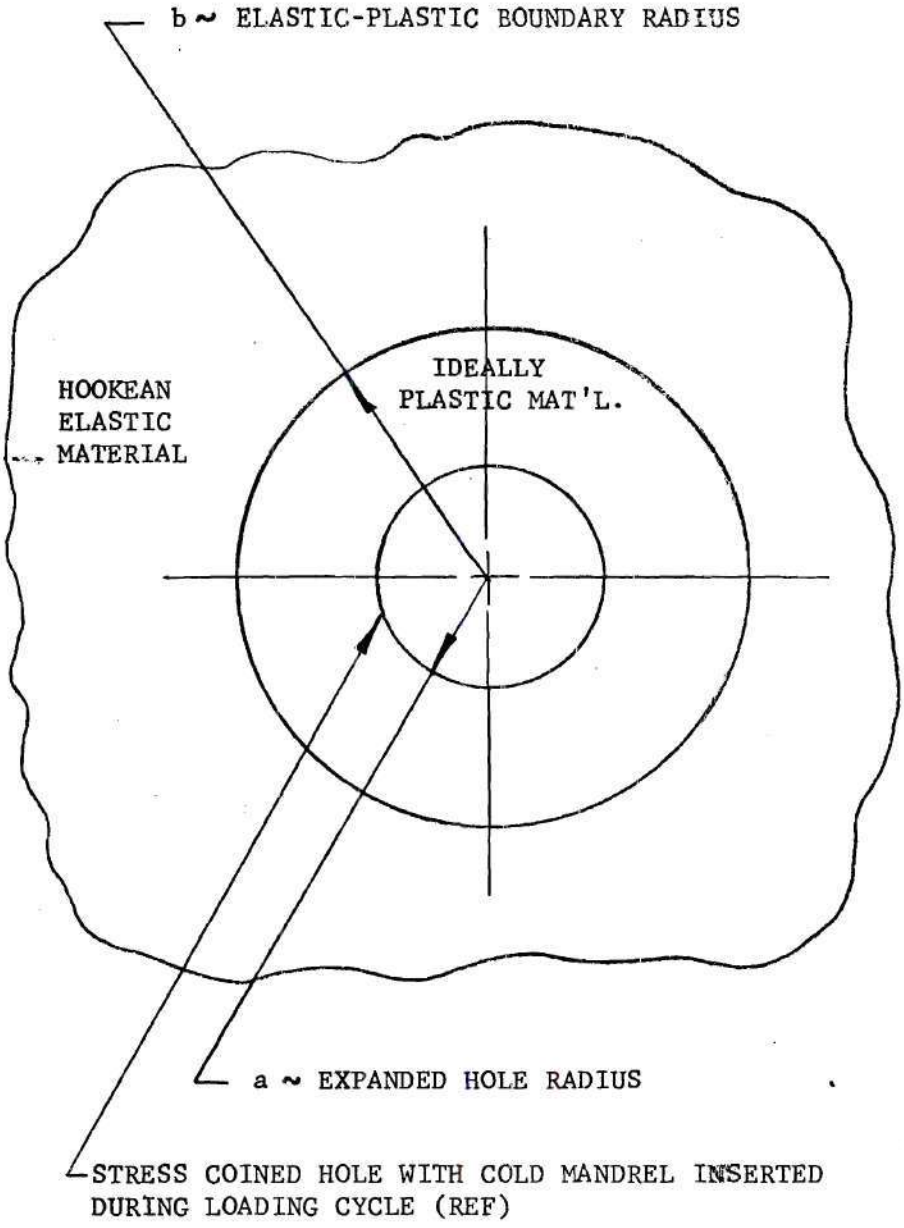

Figure 28. Schematic of Stress Coined Fastener Hole for Elastic-Plastic Analysis

$$\lim_{r\to\infty} \frac{E}{1-\nu^2}\left\{ C_3(1+\nu) - \frac{C_4}{r^2}(1-\nu)\right\} = 0 \tag{A.39}$$

$$\frac{E}{1-\nu^2} C_3(1+\nu) = 0 \tag{A.40}$$

$$C_3 = 0 \tag{A.41}$$

therefore,

$$\sigma_{r_e} = -\frac{E}{1+\nu}\frac{C_4}{r^2} \tag{A.42}$$

$$\sigma_{\theta_e} = \frac{E}{1+\nu}\frac{C_4}{r^2} \tag{A.43}$$

$$u_e = \frac{C_4}{r} \tag{A.44}$$

The Tresca Maximum Shear criterion (23) for yielding of the cold worked material is:

$$\left|\sigma_\theta - \sigma_r\right| = \sigma_y \tag{A.45}$$

Substitution of the yield condition (A.45) into the equilibrium equation (A.33) for gives

$$\frac{d\sigma_{r_p}}{dr} - \frac{\sigma_y}{r} = 0 \tag{A.46}$$

which has the general solution:

$$\sigma_{r_p} = \sigma_y \ln r + C_5 \tag{A.47}$$

Substitution of equation (A.47) into equation (A.45) gives the plastic tangential stress:

$$\sigma_{\theta_p} = \sigma_y + \sigma_y \ln r + C_5 \tag{A.48}$$

For Tresca yield condition (24), the associated plastic flow rule of the incremental type (Ref. Fung, p. 146) (25) may be written by using Koiter's generalized plastic potential:

$$d\epsilon_{\theta_p} = \lambda db \tag{A.49}$$

$$d\epsilon_{r_p} = -\lambda db \tag{A.50}$$

$$d\epsilon_{z_p} = 0 \tag{A.51}$$

Where λ is the plastic flow function and db is the incremental elastic-plastic boundary displacement, the total strain ($\epsilon_{r_{tp}}$) in the plastic region $a \leq r \leq b$ is:

$$\epsilon_{r_{tp}} = \epsilon_{r_{ep}} + \epsilon_{r_p} \tag{A.52}$$

then

$$d\epsilon_{r_{tp}} = d\epsilon_{r_{ep}} + d\epsilon_{r_p} \tag{A.53}$$

From Hooke's Law, the elastic part (ϵr_{ep}) of the total plastic

strain ($\epsilon_{r_{tp}}$) can be written as:

$$\epsilon_{r_{ep}} = \frac{1}{E}(\sigma_r - \nu\sigma_\theta) \tag{A.54}$$

$$d\epsilon_{r_{ep}} = \frac{1}{E}(d\sigma_r - \nu d\sigma_\theta) \tag{A.55}$$

Substitution of equation (A.50) and (A.55) into equation (A.53) gives:

$$d\epsilon_{r_{TP}} = \frac{1}{E}(d\sigma_r - \nu d\sigma_\theta) - \lambda db \tag{A.56}$$

similarly, $$d\epsilon_{\theta_{TP}} = \frac{1}{E}(d\sigma_r - \nu d\sigma_\theta) + \lambda db \tag{A.57}$$

Adding equations (A.56) and (A.57) gives:

$$d\epsilon_{r_{TP}} + d\epsilon_{\theta_{TP}} = \frac{1-\nu}{E}(d\sigma_r + d\sigma_\theta) \tag{A.58}$$

For boundary displacement $u_o = \eta$, let the elastic-plastic boundary $b = b(\eta)$. Then the corresponding stresses and displacements are:

$$\left.\begin{aligned}
\sigma_{r_e} &= \sigma_{r_e}(r,\eta) \\
\sigma_{\theta_e} &= \sigma_{\theta_e}(r,\eta) \\
u_e &= u_e(r,\eta) \\
\sigma_{\theta_p} &= \sigma_{\theta_p}(r,\eta) \\
\sigma_{r_p} &= \sigma_{r_p}(r,\eta) \\
u_p &= u_p(r,\eta)
\end{aligned}\right\} \tag{A.59}$$

Now, increase the boundary displacement to:

$$u_o = a + \delta a$$

Then, the corresponding changes taking place are:

$$\left.\begin{aligned} b &= b' + \delta b' \\ u_p &= u_{p'} + \delta u_{p'} \\ u_e &= u_{e'} + \delta u_{e'} \\ \sigma_{rp} &= \sigma_{rp'} + \delta\sigma_{rp'} \\ \sigma_{\theta p} &= \sigma_{\theta p'} + \delta\sigma_{\theta p'} \\ \sigma_{re} &= \sigma_{re'} + \delta\sigma_{re'} \\ \sigma_{\theta e} &= \sigma_{\theta e'} + \delta\sigma_{\theta e'} \end{aligned}\right\} \quad \text{(A.60)}$$

Now, at $r = b'$, one of the boundary conditions is:

$$\sigma_{\theta e'} - \sigma_{re'} = \sigma_y \quad \text{(A.61)}$$

or

$$\frac{2E}{1+\nu}\frac{C_4}{b'^2} = \sigma_y \quad \text{(A.62)}$$

$$C_4 = \frac{1+\nu}{2E}\sigma_y b'^2 \quad \text{(A.63)}$$

The other boundary condition at $r = b$ is:

$$\sigma_{re'} = \sigma_{rp'} \quad \text{(A.64)}$$

therefore,

$$-\frac{E}{1+\nu}\frac{C_4}{b'^2} = \sigma_y \ln b' + C_5 \quad \text{(A.65)}$$

Substitution of the value of C_4, and solving for C_5, gives:

$$C_5 = -\sigma_y \ln b' - \frac{\sigma_y}{2} \tag{A.66}$$

With C_4 and C_5 determined, the elastic-plastic displacements and stresses can be written as follows:

$$\sigma_{r_e} = -\frac{\sigma_y b'^2}{2r^2} \tag{A.67}$$

$$\sigma_{\theta_e} = \frac{\sigma_y b'^2}{2r^2} \tag{A.68}$$

$$u_e = \frac{(1+\nu)}{2E} \sigma_y \frac{b'^2}{r} \tag{A.69}$$

$$\sigma_{r_p} = \sigma_y \ln \frac{r}{b'} - \frac{\sigma_y}{2} \tag{A.70}$$

$$\sigma_{\theta_p} = \frac{\sigma_y}{2} + \sigma_y \ln \frac{r}{b'} \tag{A.71}$$

From equation (A.58)

$$d\epsilon_{\theta_{TP}} + d\epsilon_{r_{TP}} = \frac{1-\nu}{E} d(\sigma_r + \sigma_\theta) \tag{A.72}$$

i.e., $$\frac{d}{dr}(du_p) + \frac{du_p}{r} = \frac{1-\nu}{E} d(2\sigma_y \ln r - 2\sigma_y \ln b') \tag{A.73}$$

or $$\frac{d}{dr}(du_p) + \frac{du_p}{r} = \frac{1-\nu}{E}(d\sigma_r + d\sigma_\theta) \tag{A.74}$$

σ_r can change at a fixed point due to changes of η at the boundary

r = a. Also, σ_r can change as the point moves during deformation. Then, according to Hill, The Mathematical Theory of Plasticity, (26)

$$d\sigma_r = \frac{\partial \sigma_r}{\partial r} du + \frac{\partial \sigma_r}{\partial \eta} d\eta \tag{A.75}$$

Since dr = du, similarly $d\sigma_\theta$ can be obtained.

Then $$\frac{d}{dr}(du_p) + \frac{du_p}{r} = \frac{2(1-\nu)}{E}\frac{\sigma_y}{r} du_p - \frac{2\sigma_y}{b'}\frac{db'}{d\eta} d\eta \frac{(1-\nu)}{E} \tag{A.76}$$

or $$\frac{d}{dr}(du_p) + \left\{1 - \frac{2(1-\nu)}{E}\sigma_y\right\}\frac{du_p}{r} = \frac{2(1-\nu)}{E}\frac{\sigma_y}{b'}\frac{db'}{d\eta} d\eta \tag{A.77}$$

For the test specimens examined in Chapter II, $2(1-\nu)\sigma_y/E$ is equal to 0.0095 and it can be neglected when compared to 1. This is consistent with the small displacement assumption. Then

$$\frac{d(du_p)}{dr} + \frac{du_p}{dr} = \frac{2(1-\nu)}{E}\frac{\sigma_y}{b'}\frac{db'}{d\eta} d\eta \tag{A.78}$$

or $$du_p = \frac{df}{r} - \sigma_y \frac{(1-\nu)}{E}\frac{db'}{d\eta}\frac{r}{b'} d\eta \tag{A.79}$$

The boundary condition at $r = a$ is $du_p = d\eta$ (A.80)

therefore, $$d\eta = \frac{df}{a} - \sigma_y \frac{(1-\nu)}{E}\frac{db'}{d\eta}\frac{a}{b'} d\eta \tag{A.81}$$

or $$df = a\, d\eta + \sigma_y \frac{(1-\nu)}{E}\frac{db'}{d\eta}\frac{a^2}{b'} d\eta \tag{A.82}$$

then $$du_p = \frac{a}{r} d\eta + \frac{(1-\nu)}{E}\sigma_y\left(\frac{a^2}{r^2} - r\right)\frac{1}{b'}\frac{db'}{d\eta} d\eta \tag{A.83}$$

where $$db' = \frac{db'}{d\eta}\, d\eta \tag{A.84}$$

and b' is a function of η only.

$$\frac{du_p}{d\eta} = \frac{a}{r} + \sigma_y \frac{(1-\nu)}{E}\left(\frac{a^2}{r} - r\right)\frac{db'}{d\eta}\frac{1}{b'} \tag{A.85}$$

where $$u_e = u_e(r, \eta), \quad u_p = u_p(r, \eta) \tag{A.86}$$

Along r = b (η), the displacements should be continuous. Then

$$u_e(b, \eta) = u_p(b, \eta) \tag{A.87}$$

or $$du_e(b, \eta) = du_p(b, \eta) \tag{A.88}$$

Because $b = b'(\eta)$, we can write $du_e = du_p$ along r = b (η) or

$$\frac{du_e}{d\eta}\, d\eta = \frac{du_p}{d\eta}\, d\eta \quad \text{along } r = b(\eta) \tag{A.89}$$

i.e., $$\frac{a}{b'} + \frac{1-\nu}{E}\sigma_y\left(\frac{a^2}{b'} - b'\right)\frac{db'}{d\eta}\frac{1}{b'} = \frac{\sigma_y}{2E}(1+\nu)\frac{db'}{d\eta} \tag{A.90}$$

or $$\frac{db'}{d\eta}\frac{\sigma_y}{2E}\left\{(1+\nu) - 2(1-\nu)\left(\frac{a^2}{b'^2} - 1\right)\right\} = \frac{a}{b'} \tag{A.91}$$

Rearranging terms gives

$$\frac{db'}{d\eta}\frac{\sigma_y}{2E}\left\{(1+\nu) - 2(1-\nu)\frac{a^2}{b'^2} + 2(1-\nu)\right\} = \frac{a}{b'} \tag{A.92}$$

which is equal to

$$\frac{db'}{d\eta}\frac{\sigma_y}{2E}\left\{3-\nu-2(1-\nu)\frac{a^2}{b^2}\right\}=\frac{a}{b'} \tag{A.93}$$

or $$\frac{\sigma_y}{2E}\left\{(3-\nu)\frac{b'}{a}-2(1-\nu)\frac{a}{b'}\right\}db'=d\eta \tag{A.94}$$

integration yields

$$\eta = u_{o_e}+\int_a^b \frac{\sigma_y}{2E}\left\{(3-\nu)\frac{b'}{a}-2(1-\nu)\frac{a}{b'}\right\}db' \tag{A.95}$$

or $$\eta = u_{o_e}+\frac{\sigma_y}{2E}\left\{(3-\nu)\frac{a}{2}\left(\frac{b^2}{a^2}-1\right)-2(1-\nu)a\ln\frac{b}{a}\right\} \tag{A.96}$$

$$\therefore\quad u_{final}=\eta=u_{o_e}+\frac{\sigma_y}{2E}\left\{(3-\nu)\frac{a}{2}\left(\frac{b^2}{a^2}-1\right)-2(1-\nu)a\ln\frac{b}{a}\right\} \tag{A.97}$$

Substitution of:

u_{o_e} = .0005 inch

u_{final} = .003 inch

a = 0.125 inch

E = 10.3×10^6 psi

$\nu = \frac{1}{2}$

into equation (A.97) gives by iteration

$$\frac{b}{a}=2.5 \tag{A.98}$$

for the alternate immersion specimens examined in Chapter II.

Unloading

During elastic unloading, i.e., withdrawing the mandrel, the governing equations for the resulting displacements and stresses are:

$$u(r) = \begin{cases} u_p(r) + C_6 r + \frac{C_7}{r} & \text{for } a \le r \le b \\ u_e(r) + C_8 r + \frac{C_9}{r} & \text{for } b \le r \end{cases} \tag{A.99}$$

$$\sigma(r) = \begin{cases} \sigma_{r_p}(r) + \frac{E}{1-\nu^2}\left\{C_6(1+\nu) - \frac{C_7}{r^2}(1-\nu)\right\} & \text{for } a \le r \le b \\ \sigma_{r_e}(r) + \frac{E}{1-\nu^2}\left\{C_8(1+\nu) - \frac{C_9}{r^2}(1-\nu)\right\} & \text{for } b \le r \end{cases} \tag{A.100}$$

The boundary condition at $r=\infty$ remains:

$$\lim_{r\to\infty} \sigma_r(r) = 0 \tag{A.101}$$

or

$$\lim_{r\to\infty} \left\{-\frac{\sigma_y b^2}{2r^2} + C_8 r + \frac{C_9}{r^2}\right\} = 0 \tag{A.102}$$

therefore,

$$C_8 = 0 \tag{A.103}$$

The boundary condition at r = b becomes:

$$u_{r_p} = u_{r_e} \tag{A.104}$$

or

$$u_{r_b}\Big|_{r=b} + C_6 b + \frac{C_7}{b} = u_e\Big|_{r=b} + \frac{C_9}{b} \tag{A.105}$$

therefore,

$$C_6 b + \frac{C_7}{b} = \frac{C_9}{b} \tag{A.106}$$

and

$$\sigma_{r_p}(b) = \sigma_{r_e}(b) \tag{A.107}$$

or $$\sigma_{r_p}(b) + \frac{E}{1-\nu^2}\left\{C_6(1+\nu) - \frac{C_7(1-\nu)}{b^2}\right\} = \sigma_{r_e}(b) + \frac{E}{1-\nu^2}\left\{-\frac{C_9(1-\nu)}{b^2}\right\} \quad \text{(A.108)}$$

therefore, $$-C_6\frac{(1+\nu)}{(1-\nu)}b + \frac{C_7}{b} = \frac{C_9}{b} \quad \text{(A.109)}$$

From equation (A.106) and (A.109):

$$C_6 = 0 \quad \text{(A.110)}$$

and $$C_7 = C_9 \quad \text{(A.111)}$$

Therefore, since $u_{r_e} = u_{r_p}$ and $\sigma_{r_e} = \sigma_{r_p}$ @ r = b, the same expression could be used for both regions during unloading. Then,

$$\sigma_r(a) = 0 \quad \text{(A.112)}$$

or $$\sigma_{r_p}(a) - \frac{E}{1+\nu}\frac{C_7}{a^2} = 0 \quad \text{(A.113)}$$

which can be solved for C_7 as follows:

$$\sigma_y \ln\frac{a}{b} - \frac{\sigma_y}{2} - \frac{E}{1+\nu}\frac{C_7}{a^2} = 0 \quad \text{(A.114)}$$

$$C_7 = \frac{1+\nu}{E}a^2\sigma_y \ln\frac{a}{b} - \frac{1+\nu}{E}\frac{a^2}{2}\sigma_y \quad \text{(A.115)}$$

or $$C_7 = \sigma_y a^2 \frac{(1+\nu)}{E}\left(\ln\frac{a}{b} - \frac{1}{2}\right) \quad \text{(A.116)}$$

Then, the governing equations for the stresses produced after unloading are:

$$\sigma_{r\,(r)}_{\text{Residual}} = \begin{cases} \frac{\sigma_y}{2}\left(\frac{a^2}{r^2}-1\right) + \sigma_y \ln\frac{r}{b} - \frac{\sigma_y a^2}{r^2}\ln\frac{a}{b} & \text{for } a \le r \le b \\ -\frac{\sigma_y}{2}\frac{b^2}{r^2} - \sigma_y \frac{a^2}{r^2}\ln\frac{a}{b} + \sigma_y \frac{a^2}{2r^2} & \text{for } b \le r \end{cases} \quad \text{(A.117)}$$

$$\sigma_{\theta\,(r)}_{\text{Residual}} = \begin{cases} \frac{\sigma_y}{2}\left(1-\frac{a^2}{r^2}\right) + \sigma_y \ln\frac{a}{b} + \sigma_y \frac{a^2}{r^2}\ln\frac{a}{b} & \text{for } a \le r \le b \\ \frac{\sigma_y b^2}{2r^2} + \sigma_y \frac{a^2}{r^2}\ln\frac{a}{b} - \frac{\sigma_y a^2}{2r^2} & \text{for } b \le r \end{cases} \quad \text{(A.118)}$$

For the alternate immersion specimens examined in Chapter II:

At r = a,

$$\sigma_{\theta\,(a)}_{\text{Residual}} = \sigma_y \ln\frac{a}{b} + \sigma_y \frac{a^2}{a^2}\ln\frac{a}{b} \quad \text{(A.119)}$$

Since $a < b$, $\sigma_{\theta\,(a)}_{\text{Residual}}$ is compressive at r = a.

At r = b,

$$\sigma_{\theta\,(b)}_{\text{Residual}} = \frac{\sigma_y}{2}\left(1-\frac{a^2}{b^2}\right) + \sigma_y \ln\frac{b}{b} + \sigma_y \frac{a^2}{b^2}\ln\frac{a}{b} \quad \text{(A.120)}$$

$$\sigma_{\theta\,(b)}_{\text{Residual}} = 18{,}400 \text{ psi.} \quad \text{(A.121)}$$

Therefore, the maximum sustained tensile stress resulting from stress coining the holes in the test specimens examined in Chapter II is:

$$\sigma_{\theta_{\substack{\text{Maximum} \\ \text{Residual}}}} = 18{,}400 \text{ psi (tension)} \qquad \text{(A.123)}$$

BIBLIOGRAPHY

LITERATURE CITED

(1) Smith, Clarence R., "Preventing Fatigue Failures," Assembly Engineering, Hitchcock Publishing Co., Illinois, March, 1968.

(2) Speakman, E. R., "Fatigue Life Improvement Through Stress Coining Methods," 72nd Annual Meeting American Society for Testing and Materials, Atlantic City, New Jersey, June 22-27, 1969.

(3) Hills, J. F., "Advantages of Some New Fastener Systems," Society of Automotive Engineers Business Aircraft Meeting, Wichita, Kansas, April 3-5, 1968.

(4) Dieter, G. E., Mechanical Metallurgy, McGraw Hill Publishing Co., New York, 1961.

(5) Smallman, R. E., Modern Physical Metallurgy, Butterworths, 1963.

(6) Sprowls, D. O. and Brown, R. H., "Stress Corrosion Mechanisms for Aluminum Alloys," Conference of Fundamental Aspects of Stress Corrosion Cracking, September 11-15, Ohio State University, 1967.

(7) Dix, E. H., Jr., "Acceleration of the Rate of Corrosion by High Constant Stresses," Transactions, American Institute of Mining, Metallurgical, and Petroleum Engineers, Vol. 137, 1940, p.11.

(8) Champion, F. A., Corrosion Testing Procedures, 2nd Edition, John Wiley and Sons, Inc., New York, 1965, p. 133.

(9) Staehle, R. W., "Comments on the History, Engineering and Science of Stress Corrosion Cracking," Conference of the Fundamental Aspects of Stress Corrosion Cracking, September 11-15, Ohio State University, 1967.

(10) Staehle, R. W., op. cit.

(11) Liebowitz, H., "Engineering Fundamentals and Environmental Effects," Fracture, Vol. III, Academic Press, New York, 1971, pp. 645-678.

(12) Uhlig, H. H., "An Evaluation of Stress Corrosion Cracking Mechanisms," Conference of Fundamental Aspects of Stress Corrosion Cracking, September 11-15, Ohio State University, 1967.

(13) Tetelman, A. S. and McEvily, A. J., Jr., Fracture of Structural Materials, John Wiley and Sons, Inc., New York, pp. 50-57.

(14) "Laboratory Immersion Corrosion Testing," ASTM G31-72.

(15) Sprowls, D. O and Brown, R. H., op. cit.

(16) Alcoa Aluminum Handbook, Alcoa Co. of America, Pittsburgh, 1967.

(17) Backofen, W. A., Deformation Processing, Addison-Wesley Publishing Co., London, 1972, p. 105.

(18) "Stress Corrosion Test for Aluminum Alloy Plate, Extrusions, and Forgings by Alternate Immersion," Federal Test Method Standard No. 151b, Method 825, 1967.

(19) Sprowls, D. O., "Reporting and Evaluating Stress Corrosion Data," Stress Corrosion Testing, ASTM STP 425, American Society for Testing and Materials, Philadelphia, 1967.

(20) Phillips, A., Kerlins, V., and Whiteson, B. V., Electron Fractography Handbook, Technical Report ML-TDR-64-416, 1965.

(21) Phillips, A., Kerlins, V., and Whiteson, B. V., op. cit.

(22) Sprowls, D. O. and Brown, R. H., op. cit.

(23) D'isa, Frank A., Mechanics of Metals, Addison-Wesley Publishing Co., London, 1968, pp. 178-180.

(24) Prager, William, "On the Use of Singular Yield Conditions and Associated Flow Rules," Journal of Applied Mechanics, September, 1953, American Society for Testing and Materials, Philadelphia, 1953.

(25) Fung, W. C., Foundations of Solid Mechanics, Prentice-Hall, Inc. New Jersey, 1965, p. 146.

(26) Hill, R., The Mathematical Theory of Plasticity, The Clarendon Press, Oxford, 1950.